

Supporting Information

Energy Alignment and Recombination in Perovskite Solar Cells: Weighted Influence on the Open Circuit Voltage

Ilario Gelmetti^{a,b†}, Núria F. Montcada^{a†}, Ana Pérez-Rodríguez^c, Esther Barrena^{*c}, Carmen Ocal^c, Inés García-Benito^d, Agustín Molina-Ontoria^d, Nazario Martín^{d,e*}, Anton Vidal-Ferran^{a,f*}, and Emilio Palomares^{a,f*}

- a. Institute of Chemical Research of Catalonia (ICIQ). The Barcelona Institute of Science and Technology. Avda. Països Catalans, 16. Tarragona. E-43007. Spain.
- b. Departament d'Enginyeria Electrònica, Elèctrica i Automàtica, Universitat Rovira i Virgili, Avda. Països Catalans 26, 43007 Tarragona, Spain
- c. Institut de Ciència de Materials de Barcelona (ICMAB-CSIC), Campus UAB, Bellaterra 08193-Barcelona, Spain.
- d. IMDEA-Nanociencia, C/ Faraday, 9, Campus de Cantoblanco, E-28049, Madrid, Spain.
- e. Departamento de Química Orgánica I, Facultad de Ciencias Químicas, Universidad Complutense de Madrid, Madrid, Spain.
- f. ICREA. Passeig Lluís Companys, 23. Barcelona. E-08010. Spain.

Author information: EP epalomares@iciq.es

† These authors contributed equally to this work

Contents

1. Experimental details	2
2. Novel HTMs synthesis	5
3. Cyclic voltammograms in solution	13
4. Space charge limited current mobility measurements	14
5. Simulated Molecular Orbitals	15
6. Measured and Simulated UV-vis Absorbance Spectra	18
7. Determination of band gap from absorbance and photoluminescence	20
8. Surface Characterization via Alternating Current Atomic Force Microscopy (AC-AFM) and Environmental Scanning Electron Microscopy (ESEM) coupled with Energy-Dispersive X-ray analysis (EDX) 21	
9. XRD analysis of complete devices	27
10. Perovskite Layer Thickness Evaluation via Elevation Profile Measurement	28
11. Cross-sectional characterization via Scanning Electron Microscopy (SEM)	29
12. Device statistics	31
13. Forward and Reverse Current-voltage Scans for Champion Devices	33
14. Current-voltage Scans at Different Sweep Speeds	34
15. Current-voltage Scans at Different Illumination Intensities	36
16. Photo-induced time-resolve measurements	40
17. Contact potential difference measurements for work function determination	45
18. Supplementary references	46

1. Experimental details

Materials

All solvents were purchased from Sigma-Aldrich and used without any additional treatment. Formamidinium iodide (FAI) and methylammonium bromide (MABr) were bought from GreatCell Solar. PbI_2 (99 %), PbBr_2 (99.999 %) and CsI (99.999 %) were bought from Sigma-Aldrich. All of these components are stored in a nitrogen-filled glovebox. The solution for the dense TiO_2 layer was prepared using 0.65 mL of Ti(IV) isopropoxide (Sigma-Aldrich 97 %) and 0.38 mL of acetylacetone (Sigma-Aldrich) in 5 mL of ethanol. The perovskite (CsFAMAPbIBr) precursors solution was prepared dissolving 507 mg of PbI_2 , 73.4 mg of PbBr_2 , 172 mg of FAI and 22.4 mg of MABr in 0.2 mL dimethyl sulfoxide (DMSO) mixed with 0.8 mL of N,N -dimethylformamide (DMF, anhydrous). The solution was stirred at RT for 1 hour. Then 42 μL of a 1.5 M CsI solution in DMSO were added to the previous solution. Spiro-OMeTAD (1-Material) solution was prepared dissolving 72.3 mg in 1 mL of chlorobenzene (anhydrous), then 28.8 μL of 4-tert-butylpyridine (Sigma-Aldrich) and 17.5 μL of a 520 $\text{mg}\cdot\text{mL}^{-1}$ of a Lithium bis trifluoromethylsulfonyl imide (LiTFSI , Sigma-Aldrich) solution in acetonitrile were added. TAE-1 was synthesized as reported¹ and the solution was prepared using the same additives as for the spiro-OMeTAD solution, but all the molar concentrations halved due to solubility issues. TAE-3 and TAE-4 solutions were prepared with the same additives as for spiro-OMeTAD solution, but all the molar concentrations reduced to one third for TAE-3 and to one sixth for TAE-4 due to their lower solubility.

Novel HTMs synthesis and characterization

Complete synthetic procedure and characterization can be found in the SI. Flash chromatography was performed using silica gel (Merck, Kieselgel 60, 230–240 mesh or Scharlau 60, 230–240 mesh). Analytical thin layer chromatography was performed using aluminium-coated Merck Kieselgel 60 F254 plates. Oxidation potential in solution was measured with cyclic voltammetry measurements using an Autolab PGSTAT 30 electrochemical analyser at RT with a three-electrode configuration in dichloromethane containing approximately 1 mM of analyte. 0.1 M supporting electrolyte of NBu_4PF_6 was added. A glassy carbon electrode was used as working electrode, and platinum wires were used as counter and reference electrodes. Solutions were stirred and deaerated by bubbling nitrogen for a few minutes prior to each voltammetric measurement. Ferrocene was added as an internal standard; its oxidation potential in DCM was positioned at 0.7 V vs. NHE and HTMs' oxidation potential were recalculated in reference to NHE. The CV scanning rate was $100 \text{ mV}\cdot\text{s}^{-1}$. NMR spectra were recorded on a Bruker Advance 300 (^1H : 400 MHz; ^{13}C : 100 MHz) spectrometer at 298 K using partially deuterated solvents as internal standards. Coupling constants (J) are denoted in Hz and chemical shifts (δ) in ppm. Multiplicities are denoted as follows: s = singlet, d = doublet, t = triplet, m = multiplet. FT-IR spectra were recorded on a Bruker Tensor 27 (ATR device) spectrometer. Mass spectra matrix-assisted laser desorption ionization (coupled to a Time-of-Flight analyser) experiments (MALDI-TOF) were recorded on a MAT 95 thermo spectrometer and a Bruker REFLEX spectrometer, respectively. UV-Vis absorbance spectra were recorded in a Varian Cary 50 spectrophotometer. Direct optical band gap was estimated via Tauc plot of absorbance. Fluorescence measurements were carried out on a Fluorolog Horiba Jobin Yvon spectrofluorimeter equipped with photomultiplier detector, double monochromator and Xenon light source.

Device fabrication

All devices were fabricated using 1.5 x 1.5 cm FTO coated glasses (TEC7, 7 Ω /square, Pilkington FTO glass 2.2 mm thickness, Xinyan Technology Ltd, pre-patterned). The substrates were cleaned (ultrasonication) in water with Hellmanex soap, water and finally isopropanol; dried and UV/ozone treated for 20 minutes. Dense TiO_2 layer was deposited (static dispensing, 80 μL) by spin-coating using the described solution at 3000 rpm, $3000 \text{ rpm}\cdot\text{s}^{-1}$, for 60 s ($\sim 30 \text{ nm}$) over the previously cleaned FTO. Then the substrates were sintered at 500 $^\circ\text{C}$ for 30 minutes and subsequently immersed in a 40 mM TiCl_4 solution in 9 % HCl at 70 $^\circ\text{C}$ for 30 minutes, cleaned with water, with isopropanol and calcined at 500 $^\circ\text{C}$ for 30 minutes. Perovskite

precursor solution was filtered (0.2 μm , PTFE) and deposited by spin-coating (80 μL , static dispensing, first step 1000 rpm, 1000 $\text{rpm}\cdot\text{s}^{-1}$, 10 s; second step 6000 rpm, 1000 $\text{rpm}\cdot\text{s}^{-1}$, 20 s; fast crystallization was induced dynamically dispensing 50 μL of chlorobenzene on the spinning substrate 5 s before the end of the second step) obtaining a 550-600 nm thick perovskite layer. The substrates were directly transferred from the spin coater to a hot plate and annealed at 100 $^{\circ}\text{C}$ for 60 minutes. The HTM solutions (spiro-OMeTAD, TAE-1, TAE-3 or TAE-4) were filtered (0.2 μm , PTFE) and deposited by spin-coating onto the perovskite layer (60 μL , static dispensing, spiro-OMeTAD at 4000 rpm, 4000 $\text{rpm}\cdot\text{s}^{-1}$, for 30 s; TAE-1 and TAE-3 at 2000 rpm, 2000 $\text{rpm}\cdot\text{s}^{-1}$, for 30 s; TAE-4 at 1000 rpm, 2000 $\text{rpm}\cdot\text{s}^{-1}$, for 45 s) and similar HTM thickness were obtained (~ 50 nm). In order to increase the oxidative doping of the HTMs, the devices were kept 1 hour in dark in a dry air chamber. Finally, 80 nm of gold was deposited by thermal evaporation in an ultra-high vacuum chamber ($1\cdot 10^{-9}$ bar) using a shadow mask leading to 4 diodes for substrate each with an active area of 9 mm^2 . The cleaning and d-TiO_2 deposition processes were performed in a class 7 clean room. The perovskite and HTM deposition processes were performed in a nitrogen-filled glovebox while purging with a nitrogen flow for reducing the DMF and DMSO vapours concentration.

Device characterization

Current-voltage characteristics were measured using a Sun 2000 solar simulator (150 W, ABET Technologies), the proper filters of the lamp were set to simulate the AM 1.5G solar spectrum, calibrated with a silicon photodiode (NREL) to obtain 1000 $\text{W}\cdot\text{m}^{-2}$ of light intensity. Applied voltage and current were measured with a Keithley digital 2400 Source Meter (sweep speed 0.6 $\text{V}\cdot\text{s}^{-1}$, auto-scale disabled).

TPV and CE measurements were carried out using a white light LED ring LUXEON[®] Lumileds providing different light intensities, the signal is measured in an oscilloscope Yokogawa DLM2052 registering drops in voltage. The light perturbations pulses were provided by a nanosecond PTI GL-3300 nitrogen laser.

In CE, a complete device is held at open circuit conditions and irradiated using white LEDs until the steady-state is reached, in other words, until the V_{OC} of each device is completely stabilized; then the device is simultaneously short-circuited and the LEDs are switched off. The charges, which have been accumulated during the irradiation, are extracted throughout an external circuit having an oscilloscope in parallel to a known small resistance (50 Ω). The measurements are performed at different light irradiation intensities, the voltage measured across the small resistance is converted to a current (via Ohm's law) and the integration over time gives the extracted charge at different light intensities.

The current-voltage scans data acquisition was performed with open source Python code developed in-house PyPV (<https://github.com/ilario/PyPV>). The data analysis for current-voltage scans, CE and TPV was performed with open source R developed in-house (<https://github.com/ilario/photophysics-data-processing-R>).

For the morphological characterization, thicknesses were measured scratching the surface and using a calibrated profilometer (Ambios Tech. XP-1). The surface roughness characterization has been done via AFM (Pico SPM II) and processed with WSxM software.² The superficial features were further investigated via ESEM-EDX (FEI Quanta 600). Cross section images of complete devices were recorded using ESEM system FEI Quanta 600 in high vacuum (10^{-8} bar) with an accelerating voltage of 20 kV.

XRD measurements were made using a Bruker-AXS D8-Discover diffractometer equipped with parallel incident beam (Göbel mirror), vertical θ - θ goniometer, XYZ motorized stage and with a GADDS (General Area Diffraction System). Complete solar cell devices were placed directly on the sample holder and the area of interest (typically a region between two diodes, avoiding the area with the gold electrode) was selected with the aid of a video-laser focusing system. An X-ray collimator system allows to analyze areas of 500 μm . The X-ray diffractometer was operated at 40 kV and 40 mA to generate $\text{Cu K}\alpha$ radiation. The GADDS detector was a HI-STAR (multiwire proportional counter of 30x30 cm with a 1024x1024 pixel). We collected frames (2D XRD patterns) covering 15-70 $^{\circ}$ 2 θ from three different detector positions at a distance of 15 cm from the sample. The exposition time was 300 s per frame and it was chi-integrated to generate the conventional 2 θ vs. intensity diffractogram. Identification of the minerals was achieved by comparison of the XRD diffractogram with the ICDD data base (release 2007) using Diffracplus Evaluation software (Bruker 2007).

Mobility measurements via space-charge limited current

The HTM hole mobility has been estimated on a device with configuration ITO/PEDOT:PSS (25 nm)/HTM (100 nm)/Au (120 nm) from a current-voltage measurement up to 5 V. The mobility was obtained fitting the SCLC curve.^{3,4}

Work Function determination via KPFM

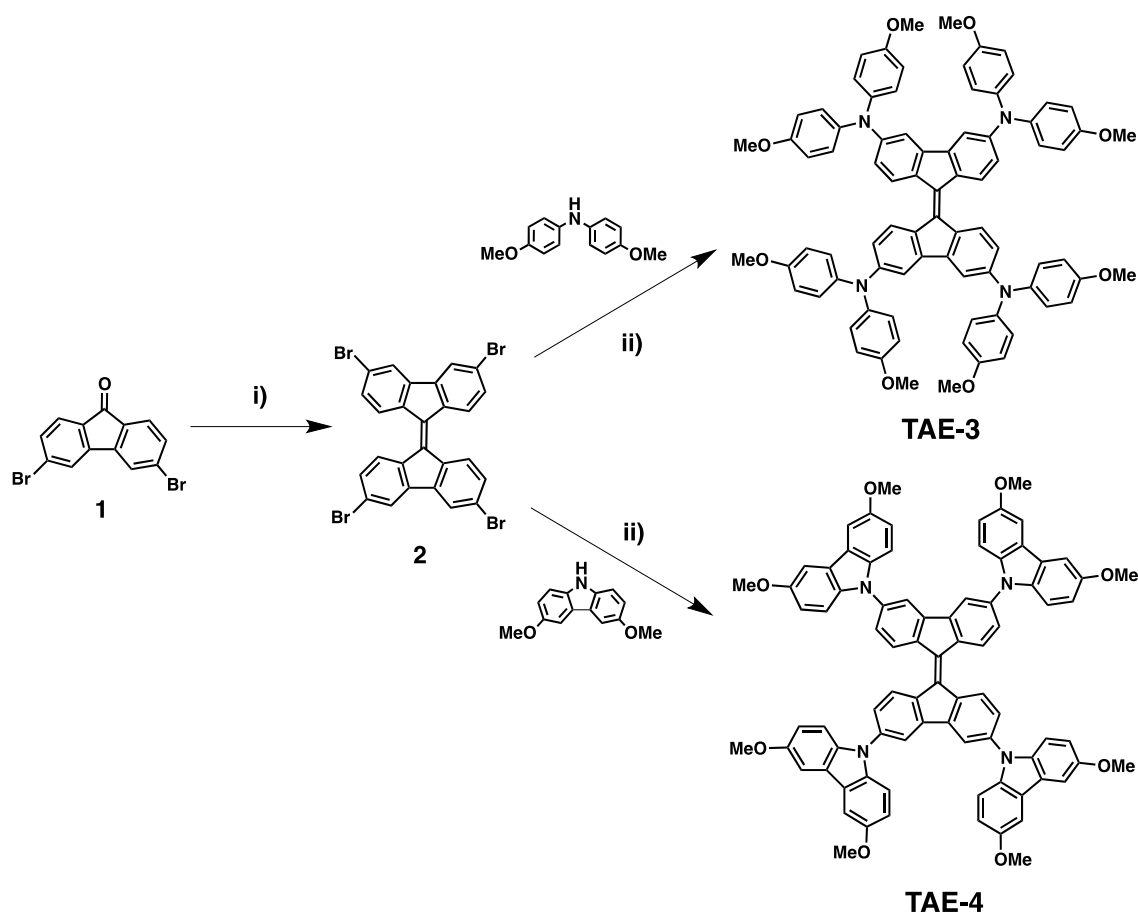
WF measurements were carried out at room temperature and under ambient conditions using a commercial scanning probe microscopy (SPM) instrument from Nanotec Electrónica. Data were analysed using the WSxM freeware.² Conducting CrPt coated Si tips (by Budgetsensors) mounted on cantilevers with nominal force constant $k = 3 \text{ N}\cdot\text{m}^{-1}$ were used. WF values were obtained by measuring the CPD between tip and sample that is determined from the parabolic dependence of the frequency shift versus bias voltage, $\Delta f(V)$ (see SI). In this work $\Delta f(V)$ curves were acquired for pristine CsFAMAPbI₃, spiro-OMeTAD/CsFAMAPbI₃ and the diverse TAEs/CsFAMAPbI₃. To avoid tip-dependent uncertainties, CPD measurements were systematically performed on grounded on-top Au electrodes (that in air conditions has been reported to be $\text{WF}_{\text{Au}} = 4.9 \text{ eV}$)⁵ deposited on each device so that a common WF reference and reproducibility were ensured. For each sample, the CPD was measured at a minimum of 15 diverse locations and 5 curves were taken at each position. As a measure of the measurements precision, the given error corresponds to the standard deviation estimated from data obtained for each case.

Theoretical simulations

In order to simulate the UVvis spectra of the three TAE compounds, full level DFT geometry optimization of TAEs were carried out using the M06-2X⁶ functional and the def2-SVP basis set⁷ as implemented in Gaussian 09, Revision D.01.⁸ The M06-2X/def2-SVP level of theory offers a good compromise between the size of the system and the accuracy of the results.⁹ Solvent effects (tetrahydrofuran) were incorporated employing the Polarizable Continuum Model (PCM) with the integral equation formalism (IEFPCM calculations)¹⁰ with radii and non-electrostatic terms¹¹ as implemented in Gaussian 09, Revision D.01. The optimized co-ordinates were used in calculation of UVvis data employing a hybrid exchange–correlation functional (CAM-B3LYP), since this methodology has proven to be reliable in UVvis predictions.¹² The CAM-B3LYP¹³ correlation functional and the previously mentioned basis set as implemented in Gaussian were used to calculate excitation energies and oscillator strengths. UVvis data obtained from computational studies were plotted using GaussSum.¹⁴

2. Novel HTMs synthesis

Compounds **1**, **2**, and **TAE-1** were prepared according to previously reported synthetic procedures^{1,15} and showed identical spectroscopic properties to those reported therein.



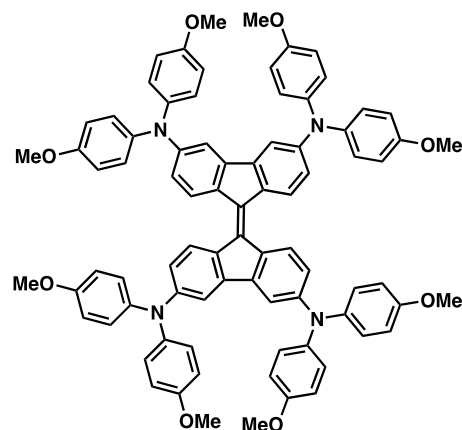
Scheme S1. Reagents and conditions: i) Lawesson's Reagent, toluene, 110°C; ii) *p*-Methoxydiphenylamine or 3,6-Dimethoxy-9H-carbazole, Pd₂(dba)₃, XPhos, Na^tBuO, toluene, 110 °C.

3,3',6,6'-Tetrakis [*N,N*-bis(4-methoxyphenyl) amino]-9,9'-bifluorenylidene, TAE-3

To a dry round bottom flask equipped with a stirrer bar, compounds **2** (100 mg, 0.16 mmol), *p*-Methoxydiphenylamine (178 mg, 0.78 mmol) XPhos (40 mg, 0.02 mmol) and Pd₂(dba)₃ (15 mg, 0.02 mmol) were dissolved in anhydrous toluene (35 mL). The resulting mixture was degassed for 30 minutes. Finally, Na^tBuO (82 mg, 0.85 mmol) was added to the solution which was heated to 100 °C for 3 hours. The reaction mixture was extracted with toluene (3 x 50 mL) and washed with water. The combined organic layers were dried over Na₂SO₄ and the solvent was removed under reduced pressure. The crude product was purified by column chromatography (silica gel, DCM and then 100:2 DCM/AcOEt).

TAE-3 was afforded as a blue solid which was washed several times

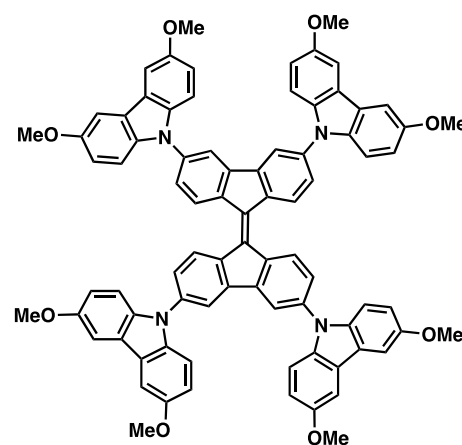
with methanol, hexane and ether (124 mg, 0.10 mmol, 63 %). ¹H NMR (400 MHz, THF-*d*₈, 298 K) δ: 7.92 (d, *J* = 8.7 Hz, 4H), 7.03 (d, *J* = 2.2 Hz, 4H), 6.96-6.82 (m, 16H), 6.77-6.64 (m, 16H), 6.54 (dd, *J* = 8.7, *J* = 2.2 Hz, 4H), 3.63 (s, 24H); ¹³C NMR (175 MHz, CDCl₃, 298K) δ 155.7, 148.4, 141.2, 141.0, 132.4, 127.0, 126.3, 119.9, 114.7, 112.3, 55.5; FTIR (neat) ν: 3042, 2996, 2937, 2834, 1598, 1557, 1504, 1448, 1320, 1270, 1237, 1176, 1116, 1034, 825, 721, 575 cm⁻¹; HRMS [MALDI-TOF] calcd. for C₈₂H₆₈N₄O₈ [M⁺], 1236.5032; found 1236.5029; elemental analysis calcd. for C₈₂H₆₈N₄O₈: C: 79.59, H: 5.54, N: 4.53; found C: 79.13, H: 5.70, N: 4.08.



3,3',6,6'-Tetrakis(3,6-dimethoxy-9H-carbazol-9-yl)-9,9'-bifluorenylidene, TAE-4.

To a dry round bottom flask equipped with a stirrer bar, compounds **2** (100 mg, 0.16 mmol), 3,6-Dimethoxy-9H-carbazole (177 mg, 0.78 mmol), XPhos (37 mg, 0.08 mmol) and Pd₂(dba)₃ (14 mg, 0.02 mmol) were dissolved in anhydrous toluene (30 mL). The resulting mixture was degassed for 30 minutes. Finally, Na^tBuO (82 mg, 0.85 mmol) was added to the solution which was heated to 100 °C for 4 hours. The reaction mixture was extracted with toluene (3 x 50 mL) and washed with water. The combined organic layers were dried over Na₂SO₄ and the solvent was removed under reduced pressure. The crude product was purified by column chromatography (silica gel, CHCl₃ and then 25:1 CHCl₃/AcOEt) to afford **TAE-4** as a purple solid (122 mg, 0.10

mmol, 62 %), which was washed several times with methanol and hexane. ¹H NMR (400 MHz, CDCl₃, 298 K) δ: 8.73 (d, *J* = 8.4 Hz, 4H), 7.95 (d, *J* = 1.9 Hz, 4H), 7.58 – 7.56 (m, 12H), 7.51 (d, *J* = 8.9 Hz, 8H), 7.07 (dd, *J* = 8.9, *J* = 2.5 Hz, 8H), 3.96 (s, 24H). ¹³C NMR (100 MHz, CDCl₃, 298 K) δ: 154.5, 142.4, 139.4, 136.8, 136.0, 128.0, 125.2, 124.3, 118.0, 115.4, 111.0, 103.2, 56.4; FTIR (neat) ν: 2937, 2828, 1608, 1465, 1432, 1328, 1289, 1202, 1159, 1106, 1038, 913, 827, 788, 669, 585 cm⁻¹; HRMS [MALDI-TOF] calcd. for C₈₂H₆₀N₄O₈ [M⁺], 1228.4406; found 1228.4446; elemental analysis calcd. for C₈₂H₆₀N₄O₈: C: 80.11, H: 4.92, N: 4.56; found C: 79.94, H: 5.04, N: 4.31.



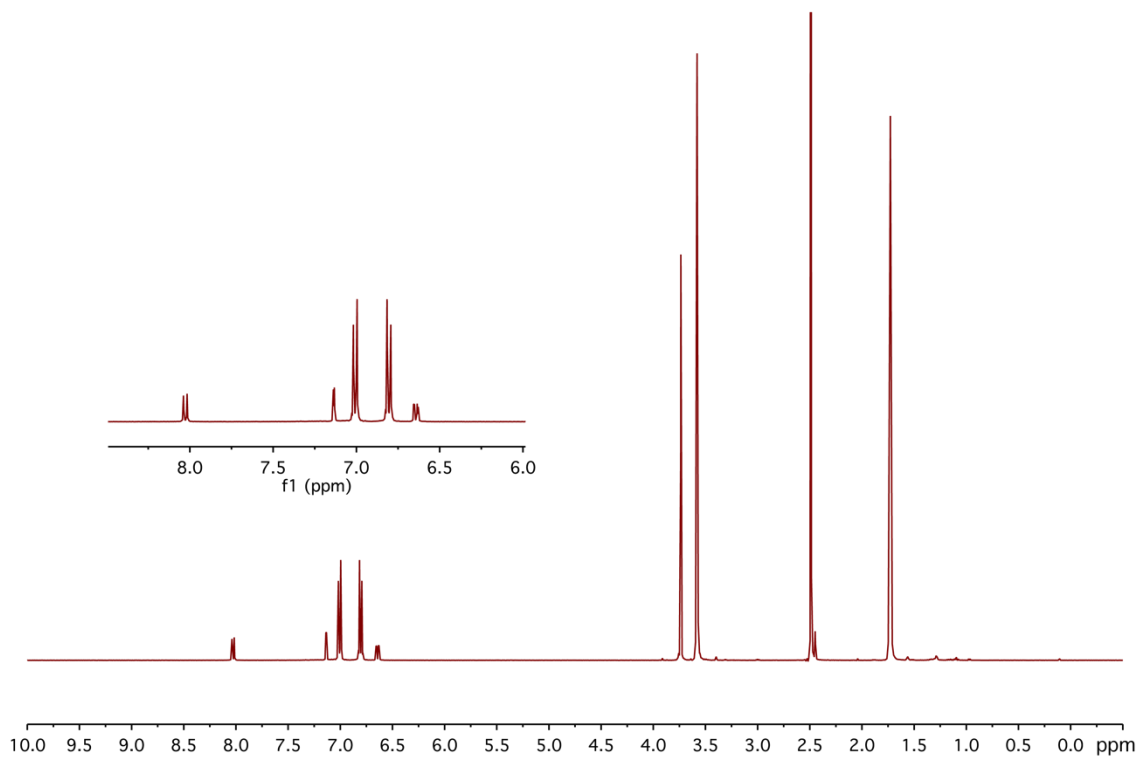


Figure S 1. ^1H NMR (400 MHz, THF-d_8 , 298 K) of TAE-3.

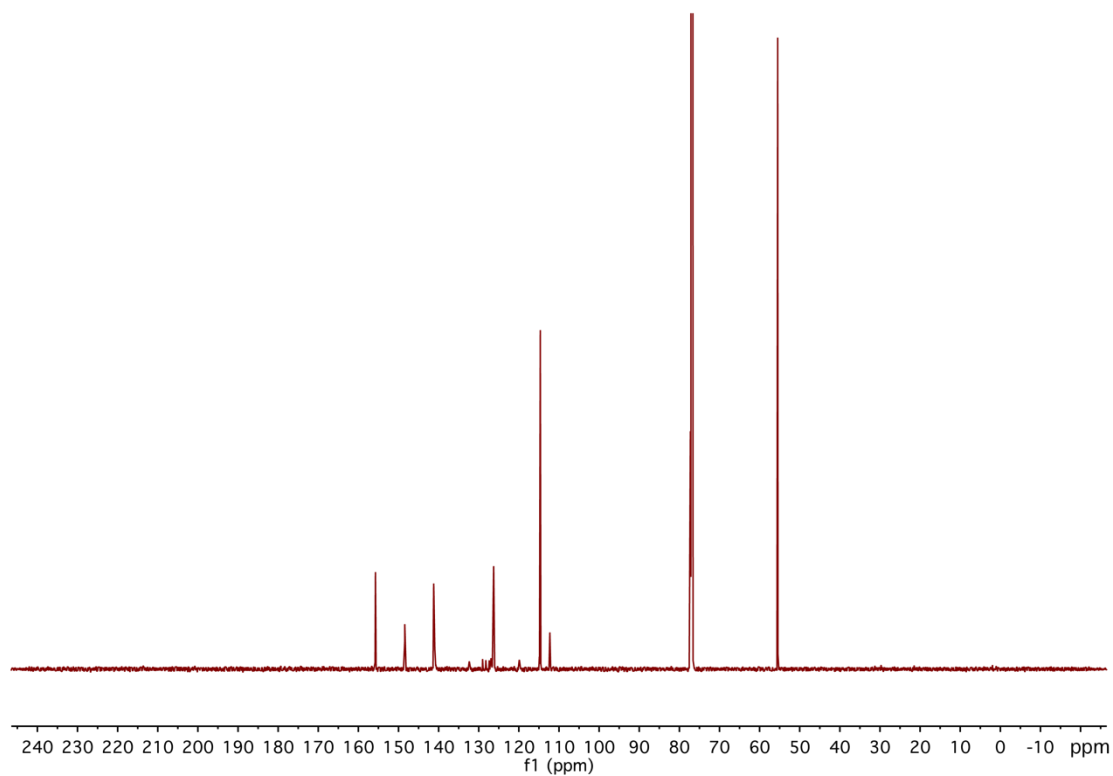


Figure S 2. ^{13}C NMR (175 MHz, CDCl_3 , 298 K) of TAE-3.

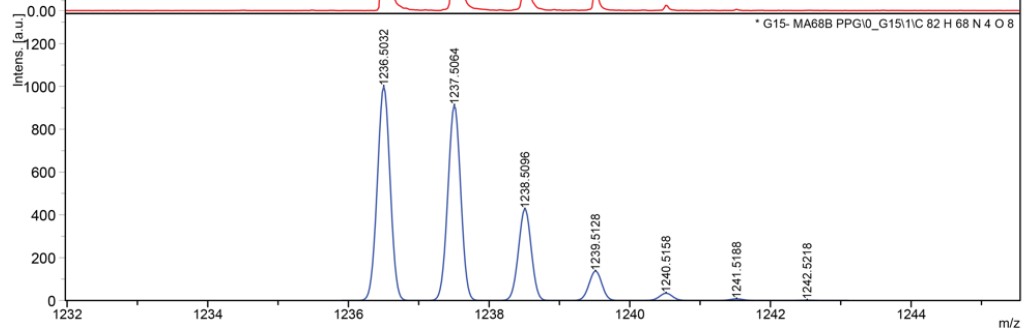
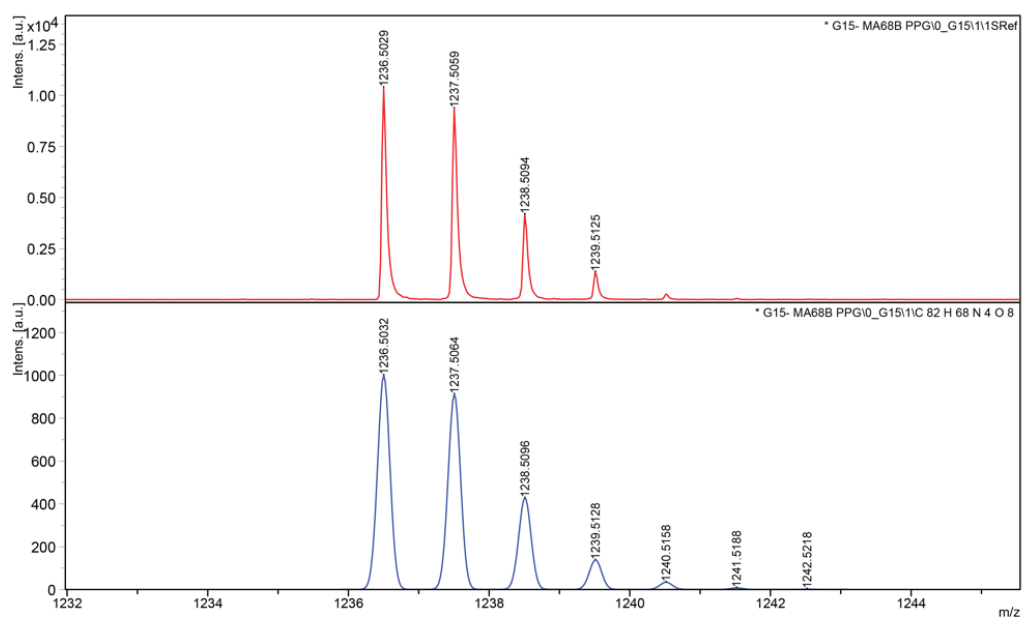
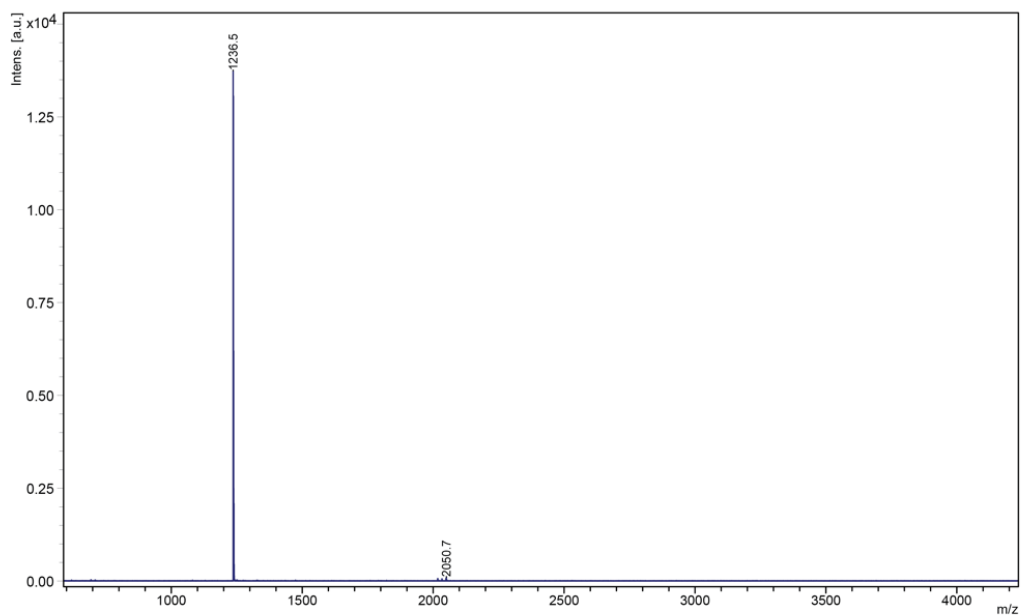


Figure S 3. HR-MALDI-TOF mass spectrum of **TAE-3**.

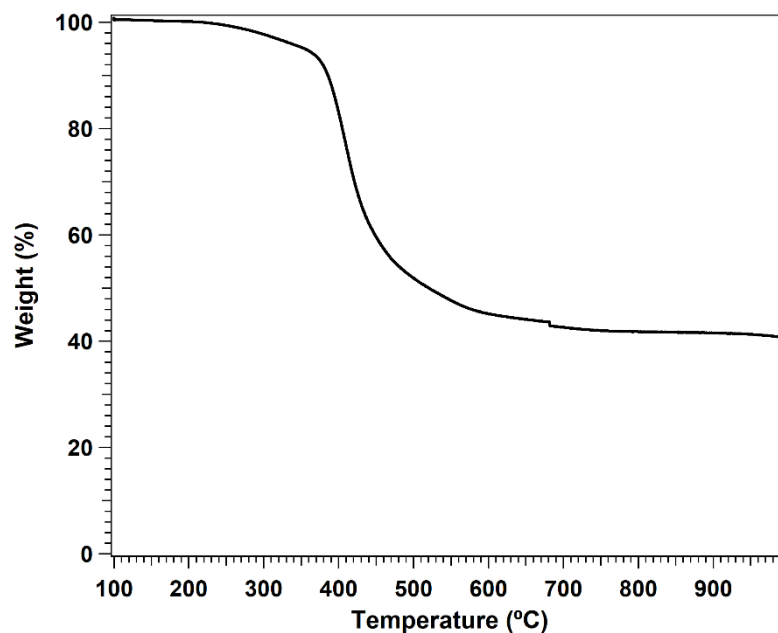


Figure S 4. Thermogravimetric Analysis of TAE-3 at scan rate of 10 °C/min.

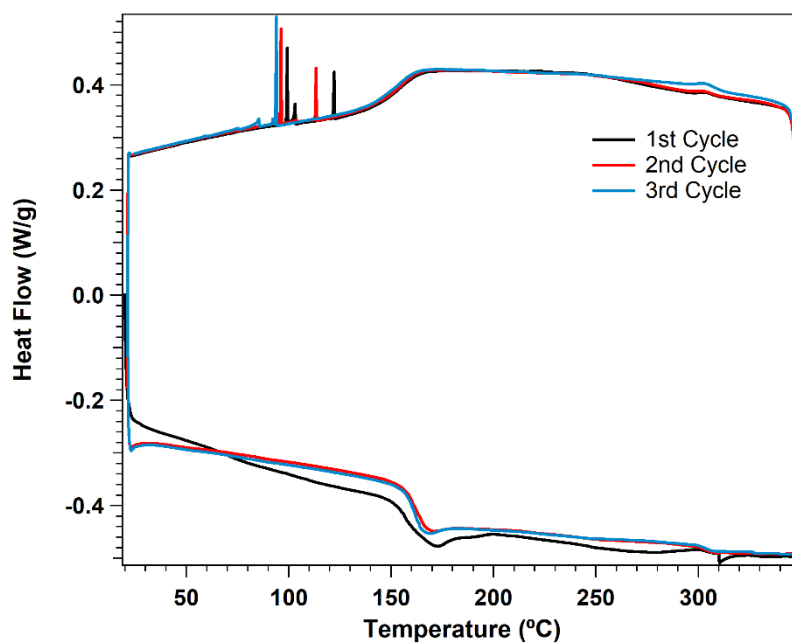


Figure S 5. Differential Scanning Calorimetry of TAE-3 at scan rate of 20 °C/min.

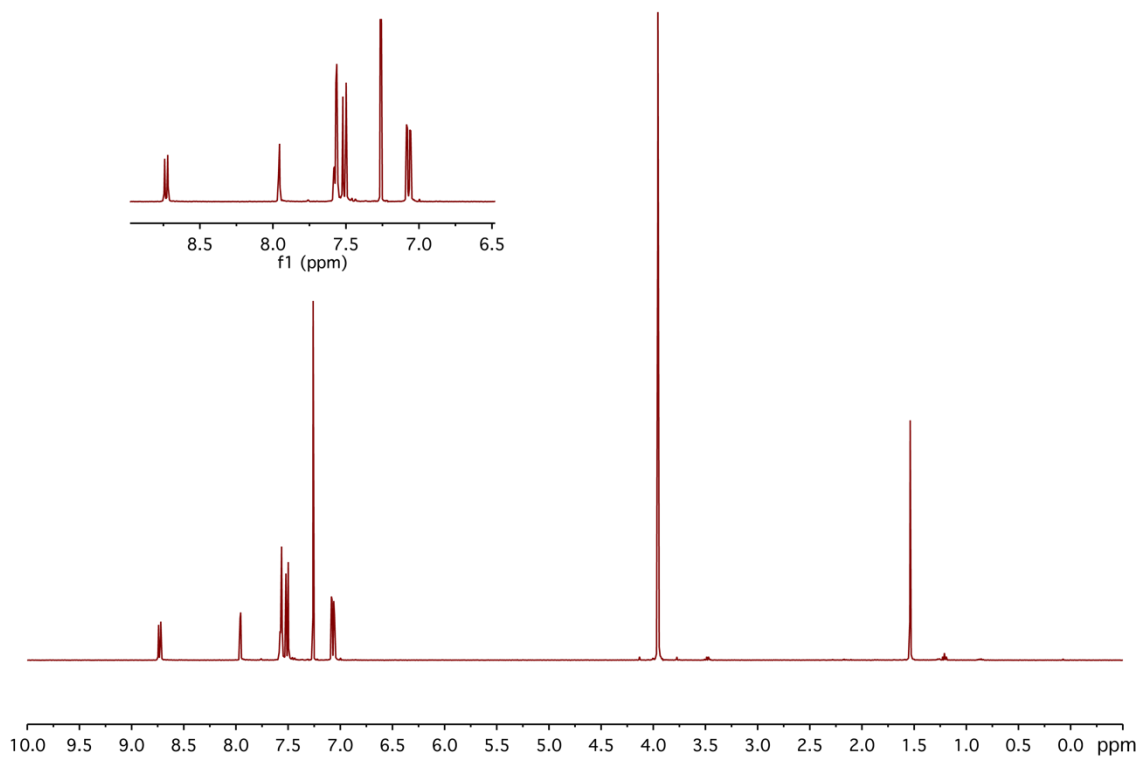


Figure S 6. ^1H NMR (400 MHz, CDCl_3 , 298 K) of TAE-4.

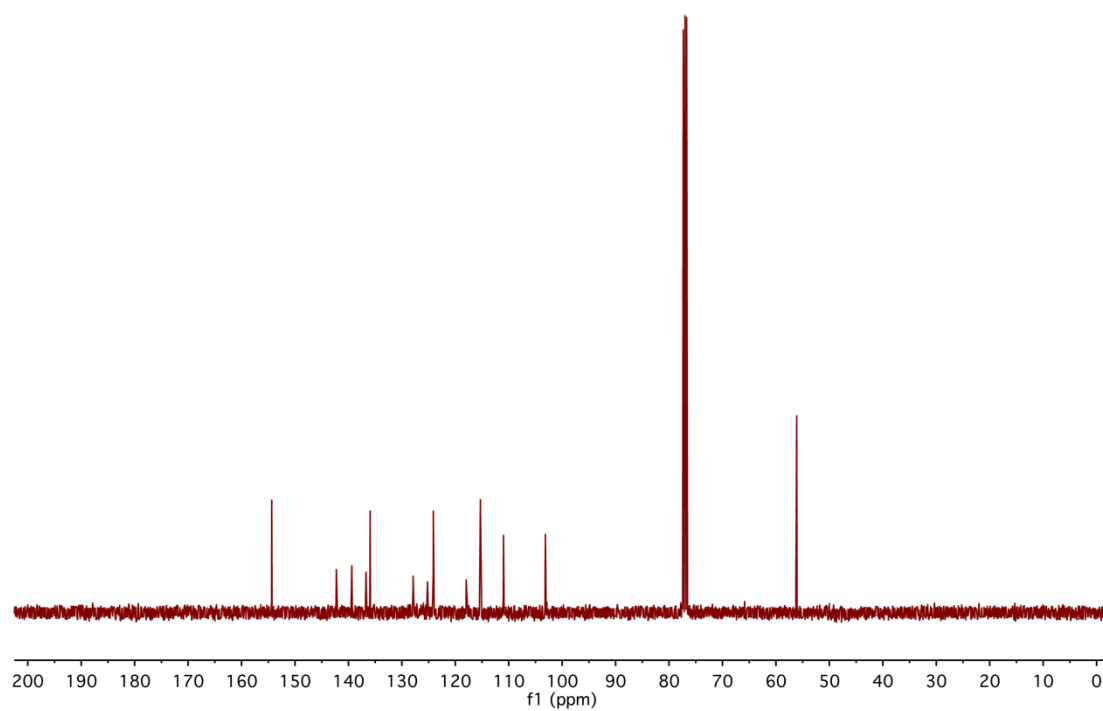


Figure S 7. ^{13}C NMR (100 MHz, CDCl_3 , 298 K) of TAE-4.

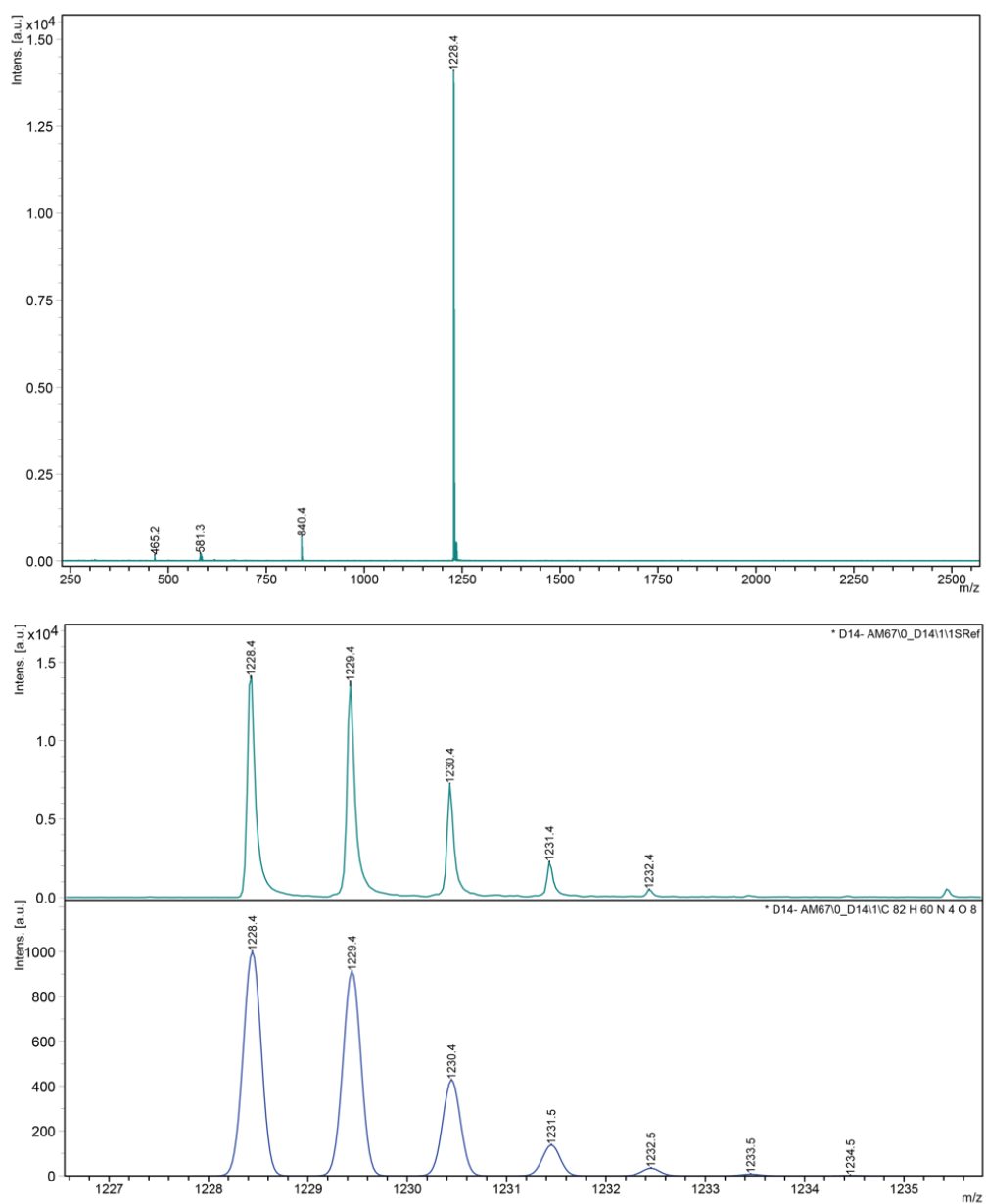


Figure S 8. HR-MALDI-TOF mass spectrum of TAE-4.

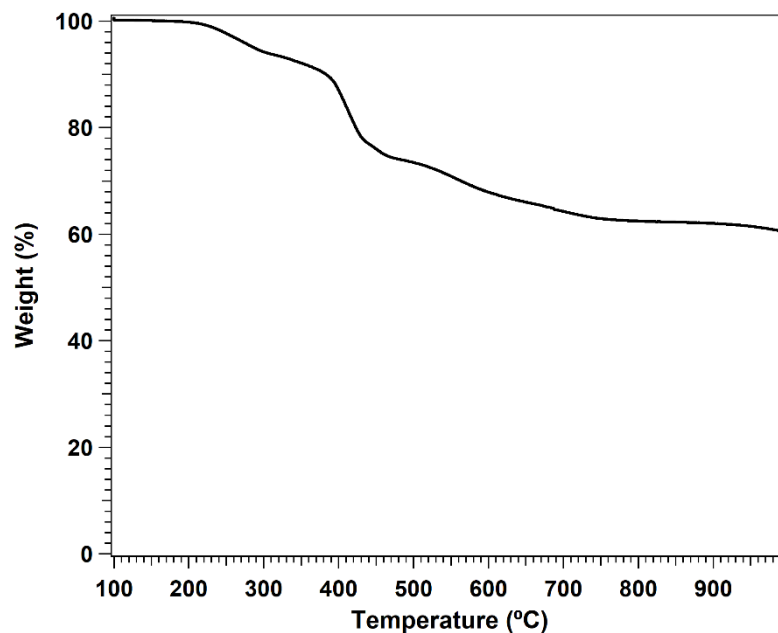


Figure S 9. Thermogravimetric Analysis of **TAE-4** at scan rate of 10 °C/min.

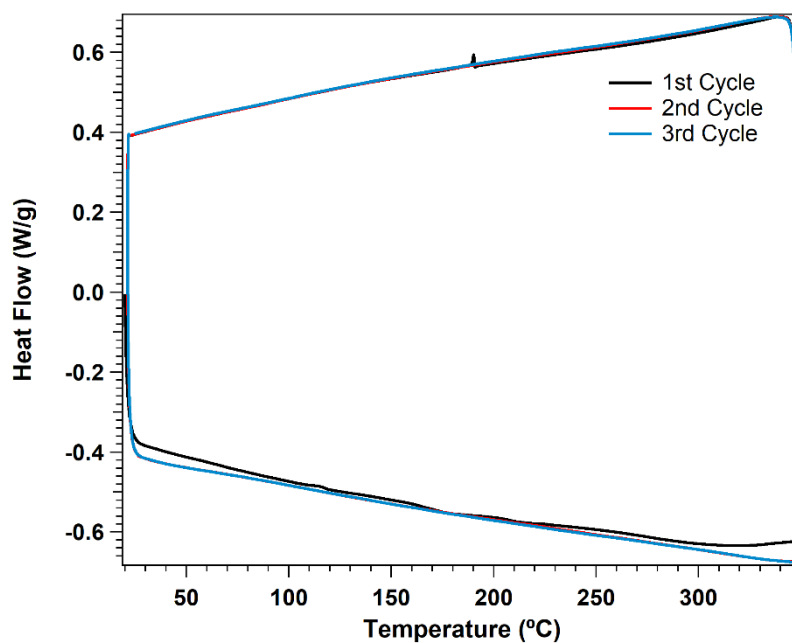


Figure S 10. Differential Scanning Calorimetry of **TAE-4** at scan rate of 20 °C/min.

3. Cyclic voltammograms in solution

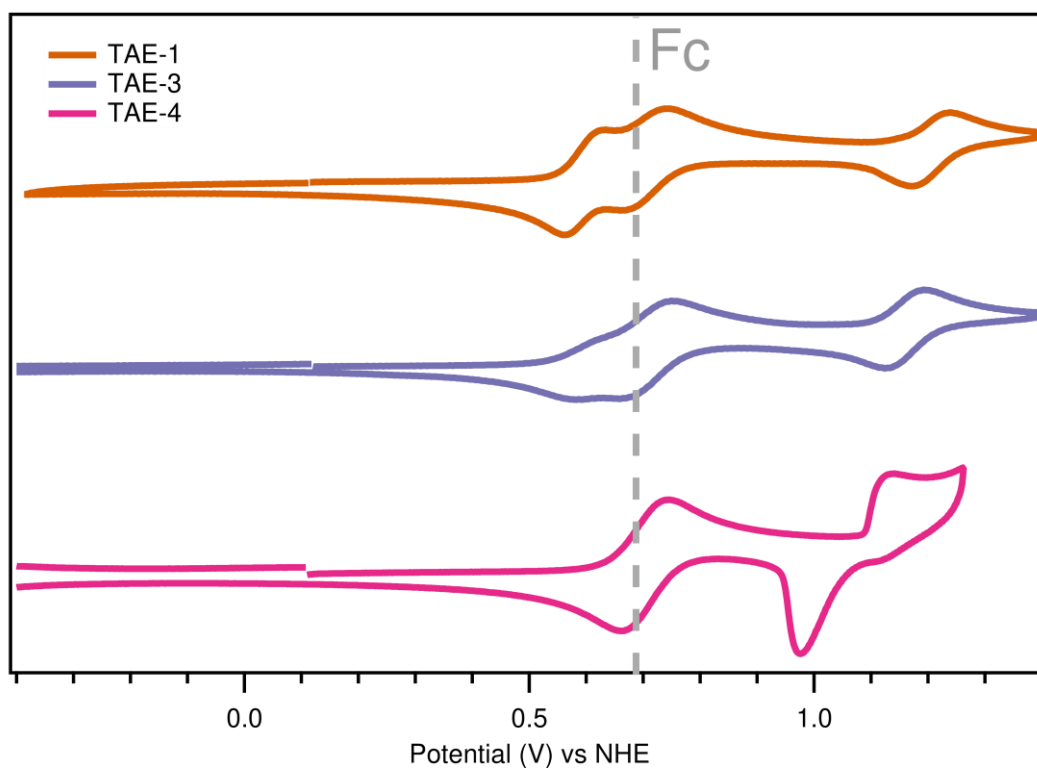


Figure S 11. Cyclic voltammogram of TAE-1, TAE-3 and TAE-4 in DCM including ferrocene and referred to NHE potential.

4. Space charge limited current mobility measurements

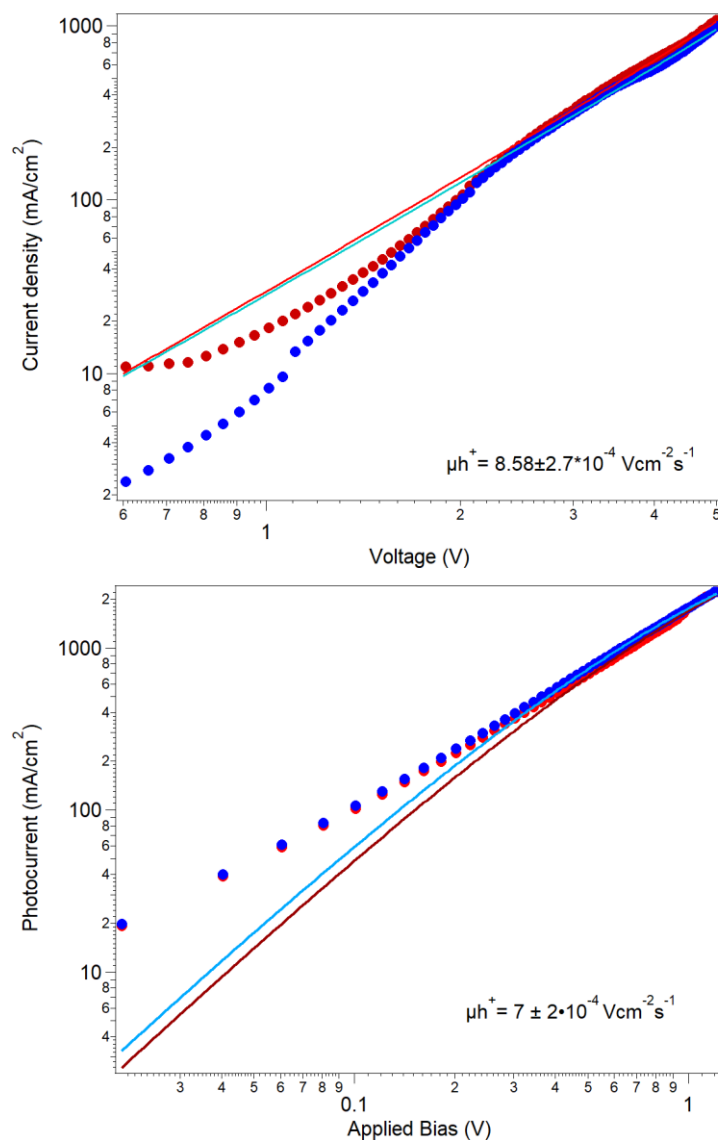


Figure S 12. Hole only (above) TAE-3 and (below) TAE-4 devices J-V at space charge limited conditions. The red symbols correspond to the measurement under illumination and the blue symbols correspond to the measurement in dark.

5. Simulated Molecular Orbitals

Table S 1. Simulated energies for HOMO and LUMO levels, their difference and the direct optical band gap as determined via Tauc plot of simulated absorbance spectra.

HTM	HOMO (eV)	LUMO (eV)	HOMO-LUMO gap (eV)	Optical BG (eV)
TAE-1	-5.61	-0.54	5.07	3.04
TAE-3	-5.54	-1.77	3.77	2.02
TAE-4	-6.14	-2.27	3.87	2.20

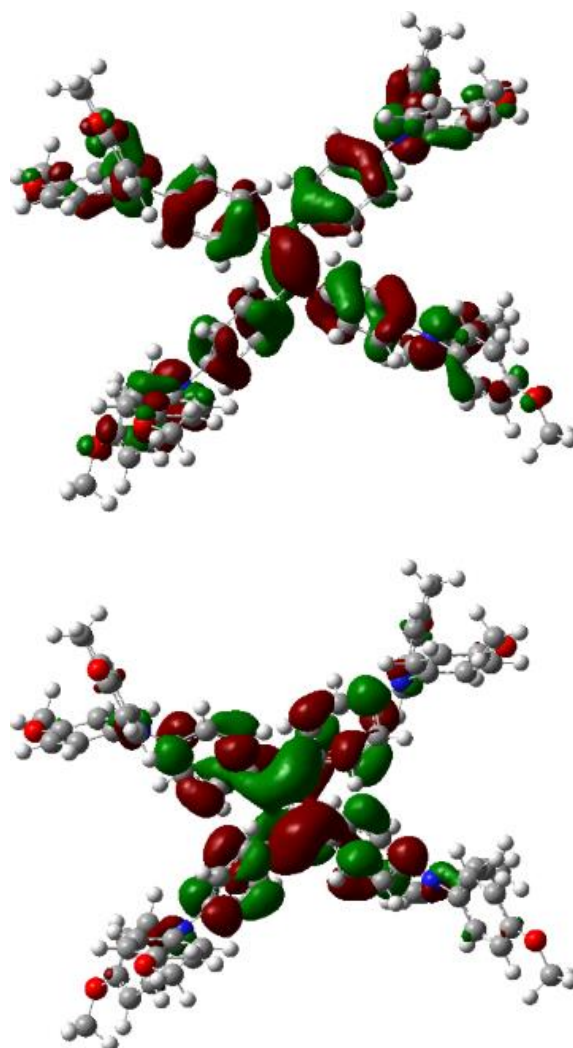


Figure S 13. Representation of the highest occupied (top) and lowest unoccupied (bottom) molecular orbitals (isovalue 0.02) for **TAE-1**.

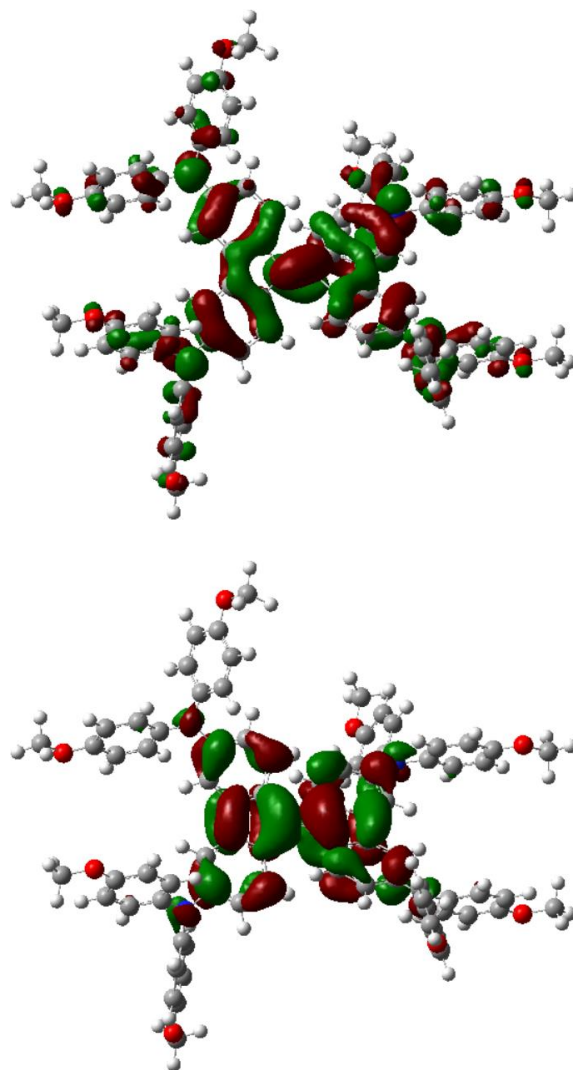


Figure S 14. Representation of the highest occupied (top) and lowest unoccupied (bottom) molecular orbitals (isovalue 0.02) for **TAE-3**.

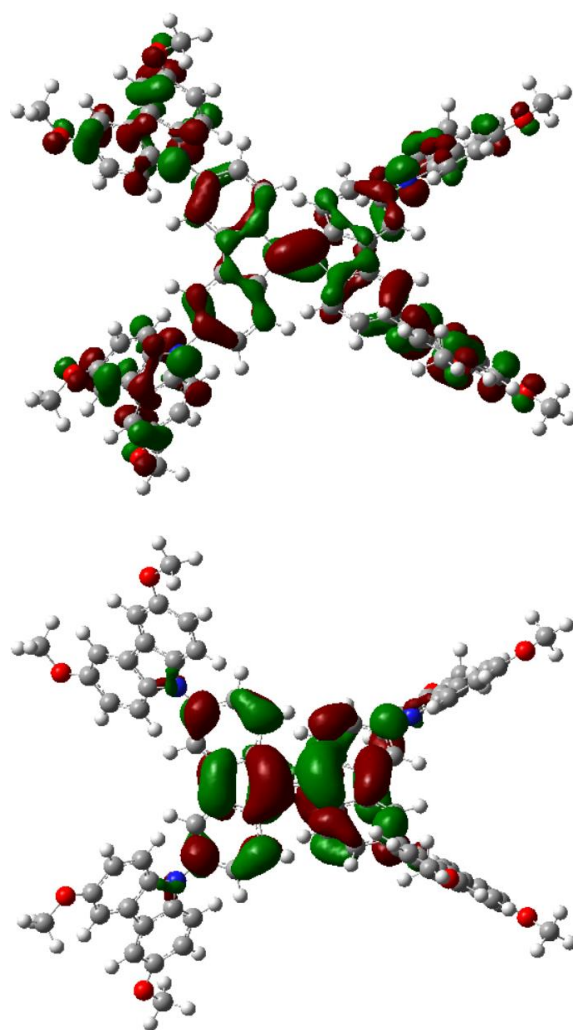


Figure S 15. Representation of the highest occupied (top) and lowest unoccupied (bottom) molecular orbitals (isovalue 0.02) for **TAE-4**.

6. Measured and Simulated UV-vis Absorbance Spectra

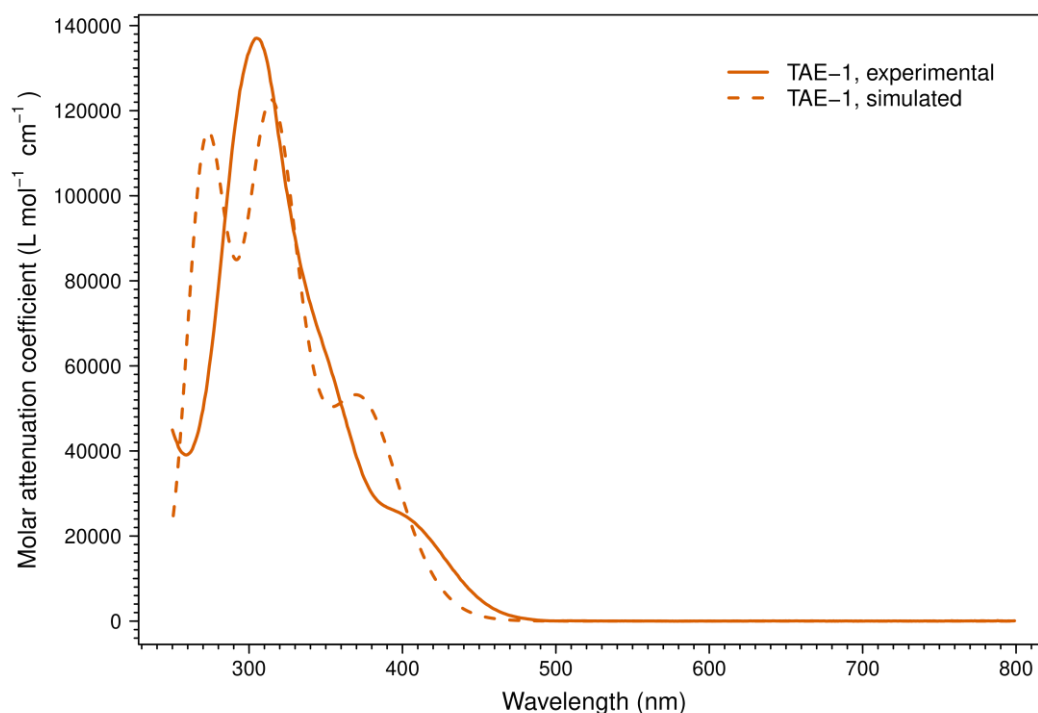


Figure S 16. Experimental (solid line) and simulated (dashed line, using a standard deviation for gaussian peaks of 4000 cm^{-1}) absorbance spectrum of **TAE-1** in THF solution.

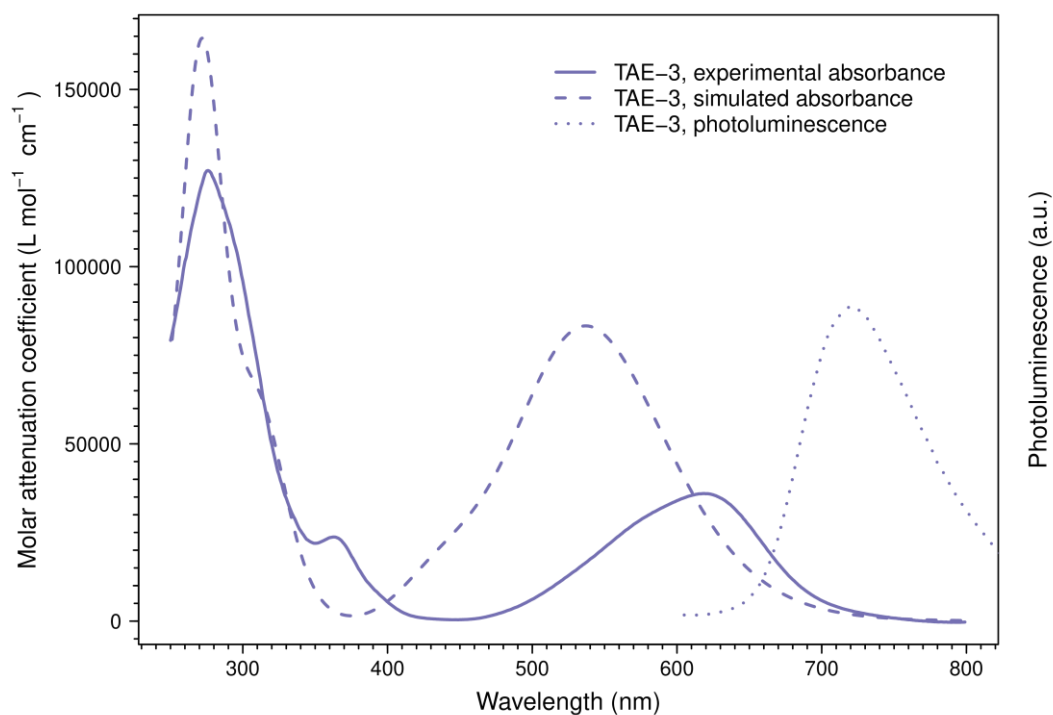


Figure S 17. Photoluminescence (dotted line, excitation wavelength 550 nm), experimental absorbance (solid line) and simulated absorbance (dashed line, using a standard deviation for gaussian peaks of 4000 cm^{-1}) spectrum of **TAE-3** in THF solution.

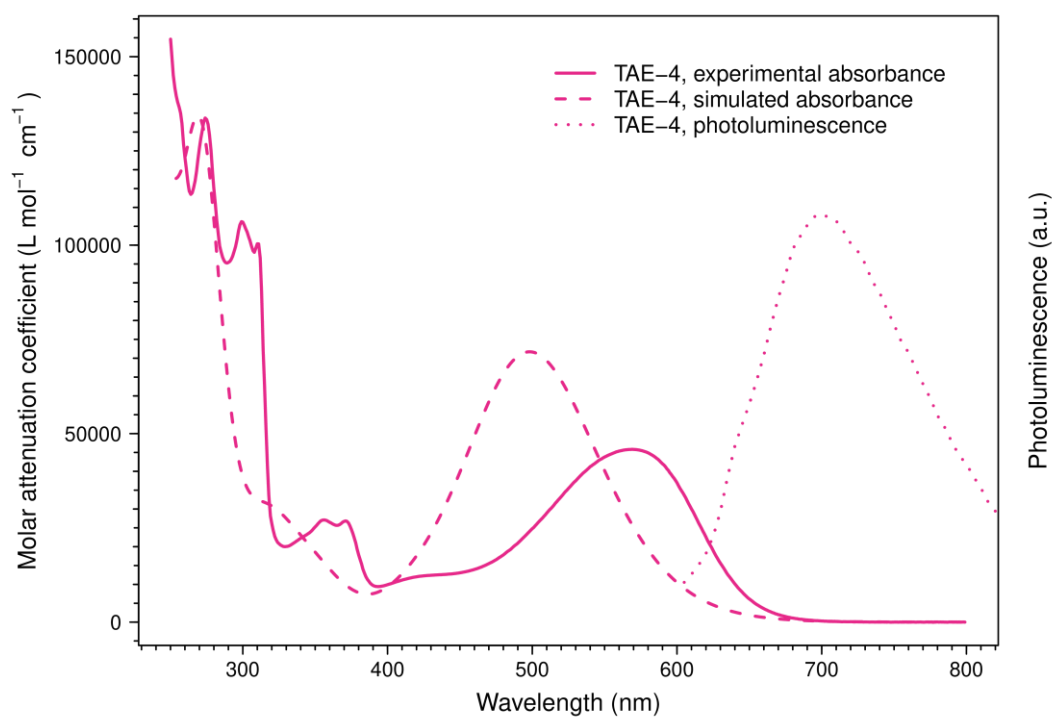


Figure S 18. Photoluminescence (dotted line, excitation wavelength 550 nm), experimental absorbance (solid line) and simulated absorbance (dashed line, using a standard deviation for gaussian peaks of 4000 cm^{-1}) spectrum of **TAE-4** in THF solution.

7. Determination of band gap from absorbance and photoluminescence

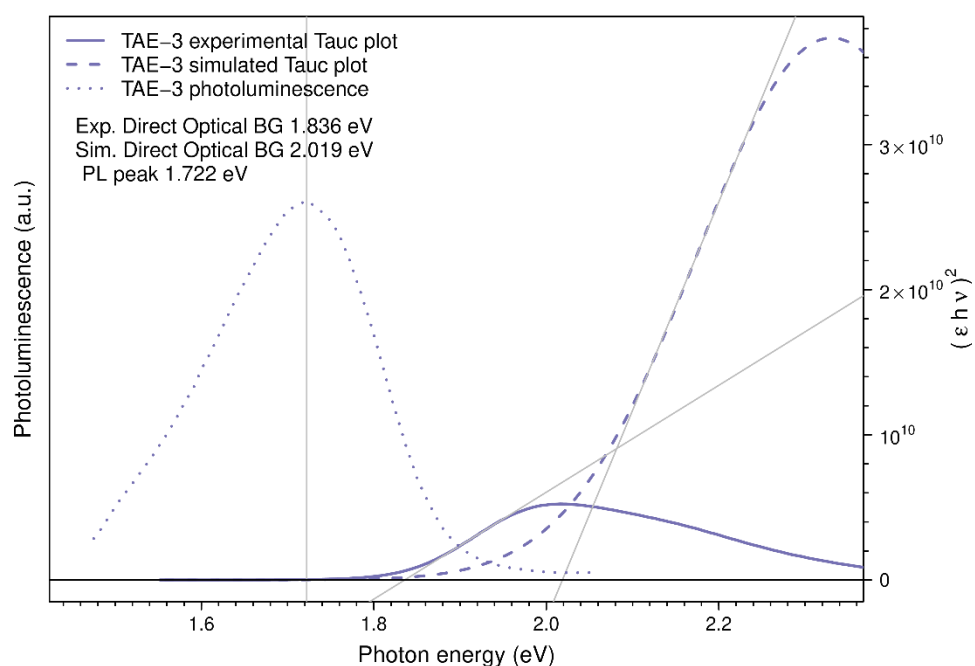


Figure S 19. Photoluminescence (dotted line, excitation wavelength 550 nm) and Tauc plot for direct optical band gap (solid line: from experimental absorbance; dashed line: from simulated absorbance) of **TAE-3** molecule in THF.

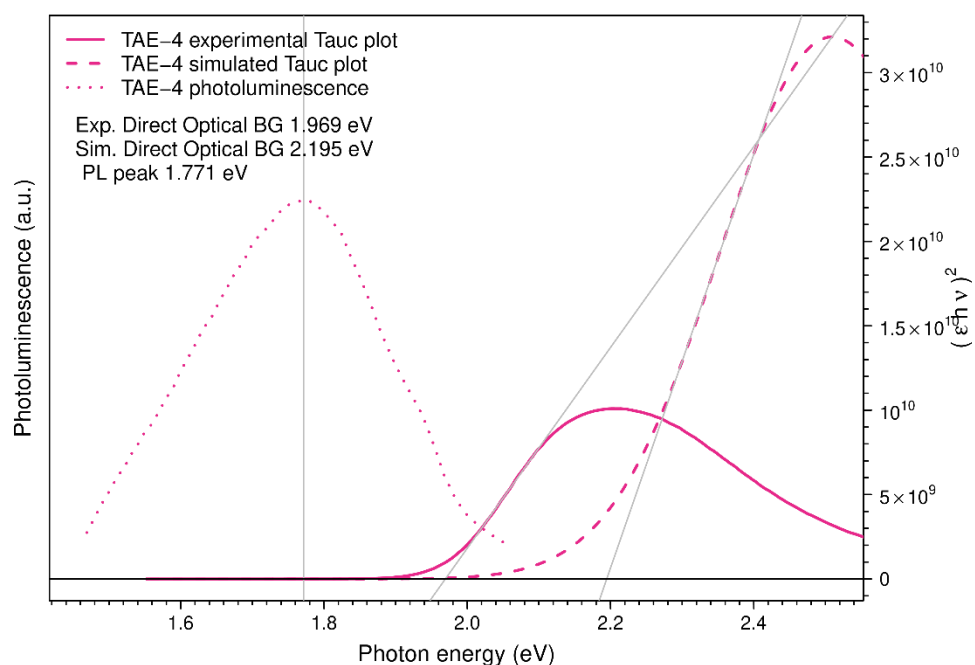


Figure S 20. Photoluminescence (dotted line, excitation wavelength 550 nm) and Tauc plot for direct optical band gap (solid line: from experimental absorbance; dashed line: from simulated absorbance) of **TAE-4** molecule in THF.

8. Surface Characterization via Alternating Current Atomic Force Microscopy (AC-AFM) and Environmental Scanning Electron Microscopy (ESEM) coupled with Energy-Dispersive X-ray analysis (EDX)

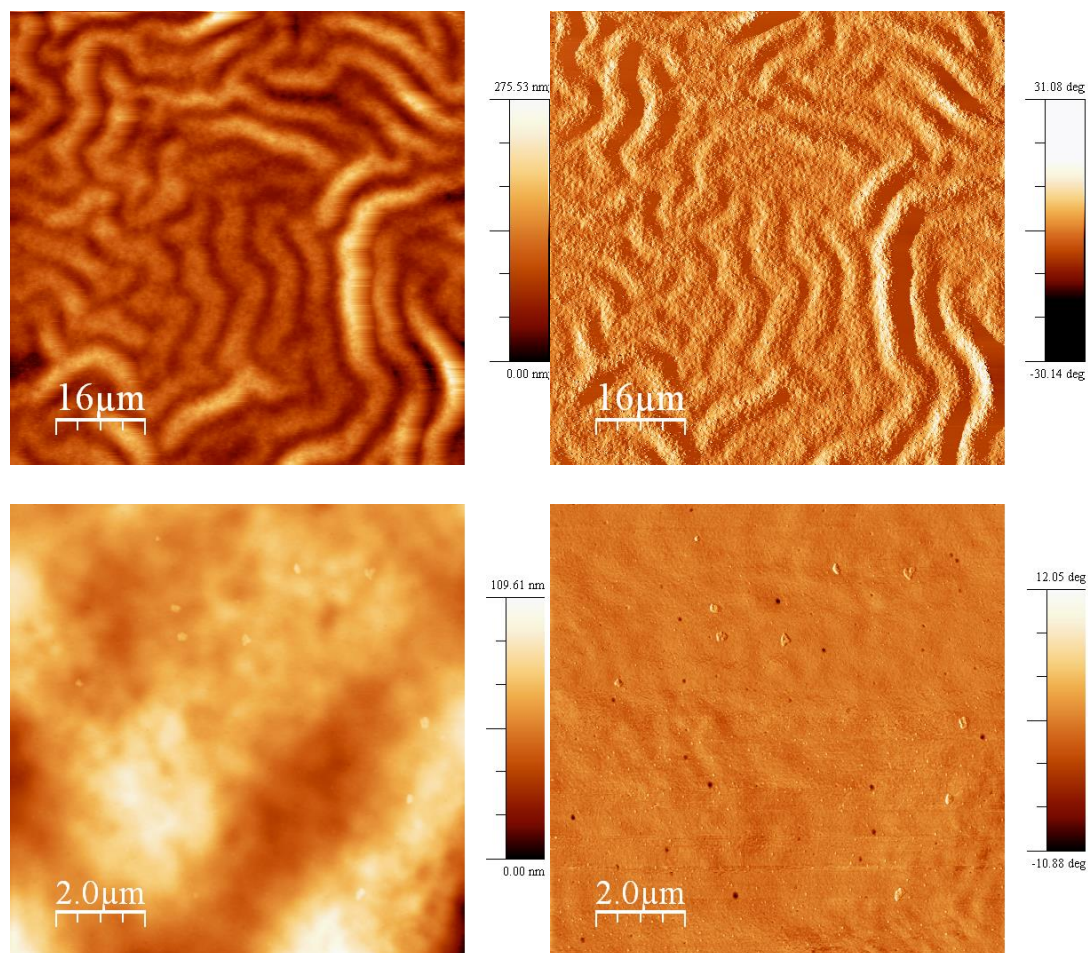


Figure S 21. AC-AFM images of spiro-OMeTAD surface in complete devices. Topography in the images on the left hand side and phase in the images on the right hand side. From the 80x80 micrometre area topography in the top image, a roughness average of $R_a = 24$ nm and a root mean square average roughness of $RMS = 31$ nm can be obtained. From the 10x10 micrometre area topography in the bottom image, a roughness average of $R_a = 10$ nm and a root mean square average roughness of $RMS = 13$ nm can be obtained.

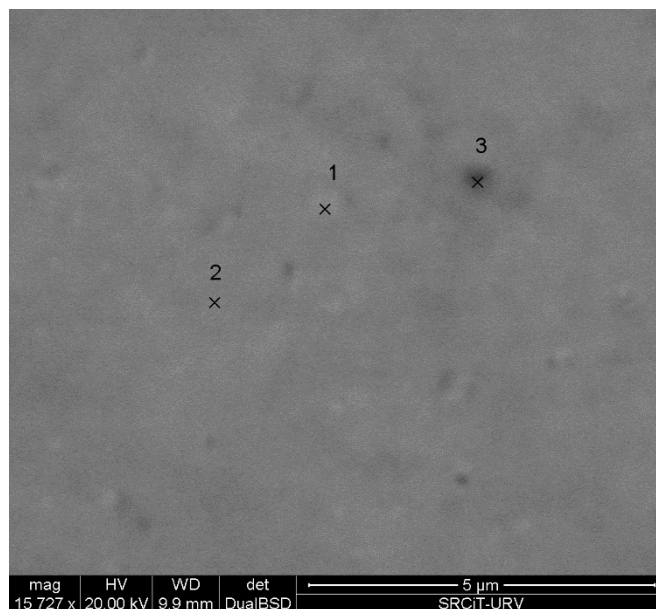


Figure S 22. ESEM imaging of the spiro-OMeTAD surface in a complete device. The three marked positions were analysed by EDX as reported in **Figure S 23**. The three locations were chosen as representative of the interesting features observed in the AC-AFM topography: position 1 is on an extruding feature, position 2 is in the flat surface and position 3 is in a hole.

Table S 2. Elemental analysis in atomic percentages as represented in Figure S 23 of the three points indicated in Figure S 22.

Element	C	O	Ti	Br	Sn	I	Pb
Position 1	30.12	16.29	2.53	4.29	13.61	24.52	8.64
Position 2	51.35	10.97	2.07	3.06	10.99	15.85	5.72
Position 3	45.74	14.34	2.47	2.89	13.91	15.32	5.35

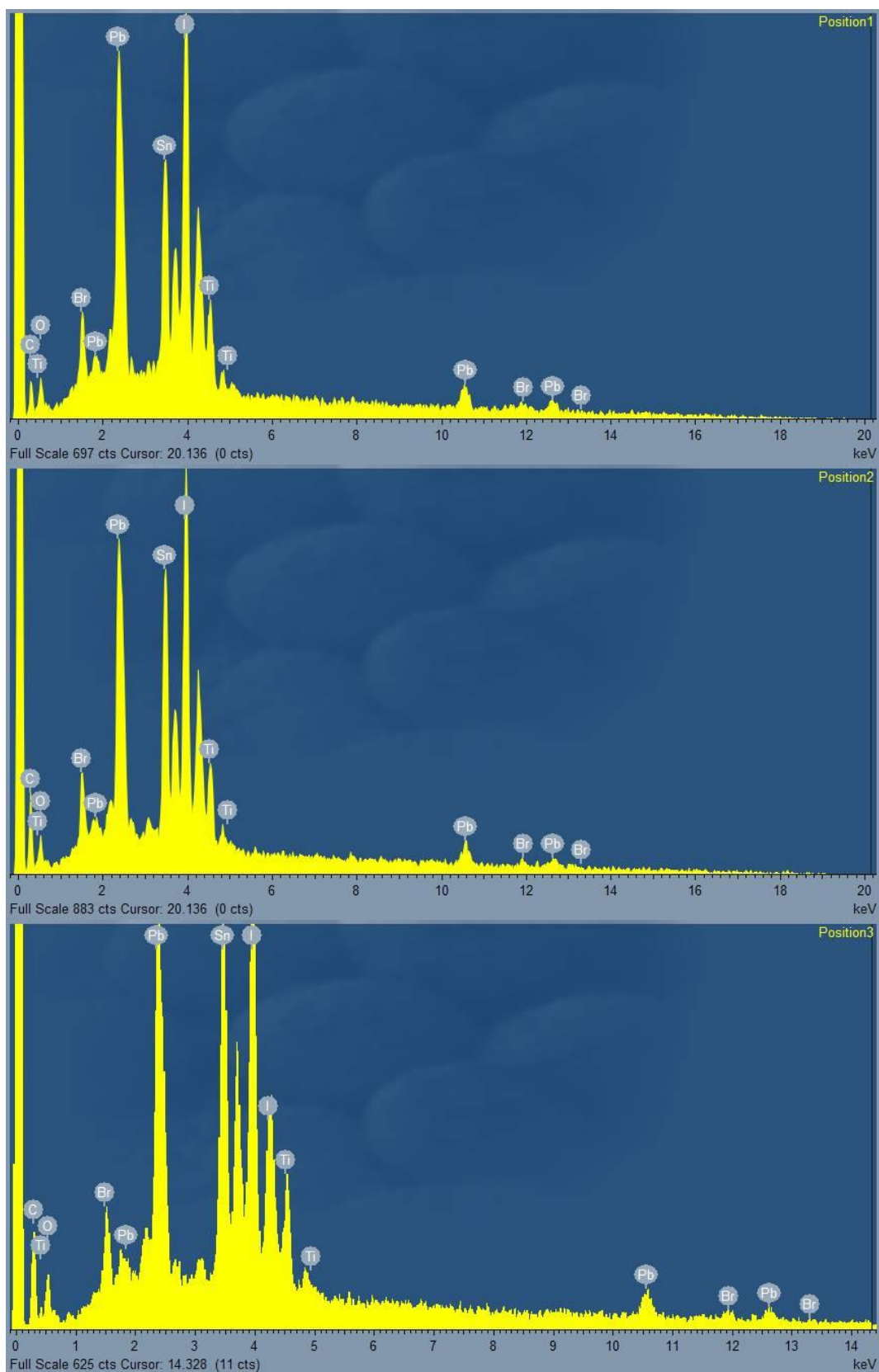


Figure S 23. EDX analysis of the three locations marked in Figure S 22. The elemental analysis is reported in Table S 2.

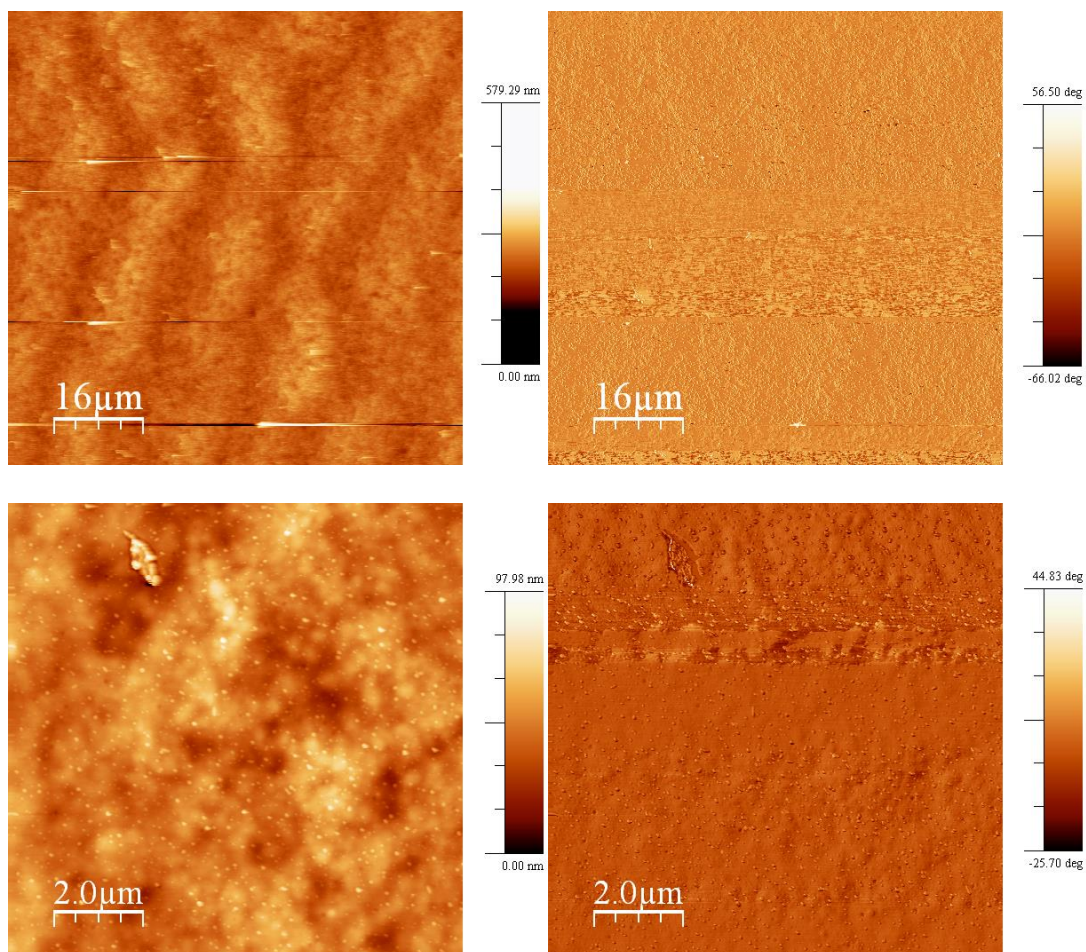


Figure S 24. AC-AFM images of TAE-1 surface in complete devices. Topography in the images on the left hand side and phase in the images on the right hand side. From the 80x80 micrometre area topography in the top image, a roughness average of $R_a = 20$ nm and a root mean square average roughness of $RMS = 30$ nm can be obtained. From the 10x10 micrometre area topography in the bottom image, a roughness average of $R_a = 8$ nm and a root mean square average roughness of $RMS = 10$ nm can be obtained.

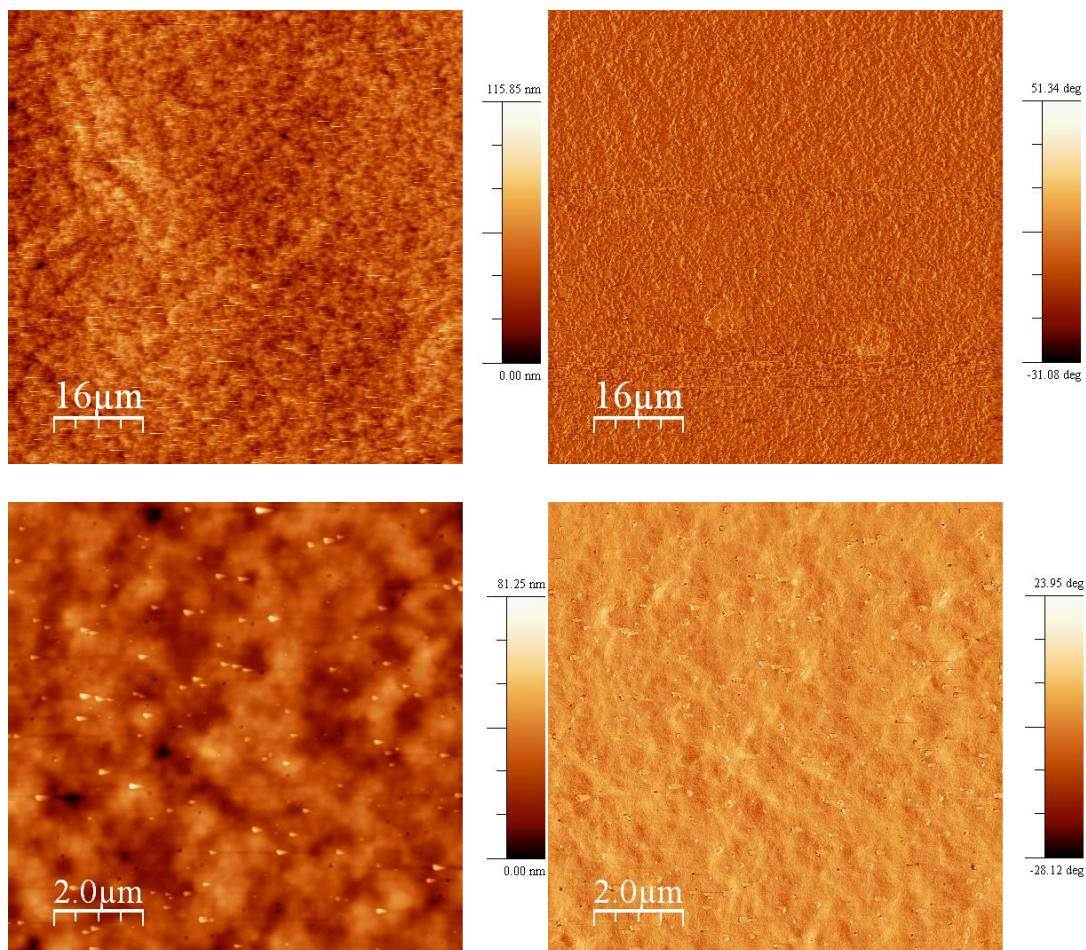


Figure S 25. AC-AFM images of TAE-3 surface in complete devices. Topography in the images on the left hand side and phase in the images on the right hand side. From the 80x80 micrometre area topography in the top image, a roughness average of $R_a = 8$ nm and a root mean square average roughness of $RMS = 10$ nm can be obtained. From the 10x10 micrometre area topography in the bottom image, a roughness average of $R_a = 6$ nm and a root mean square average roughness of $RMS = 8$ nm can be obtained.

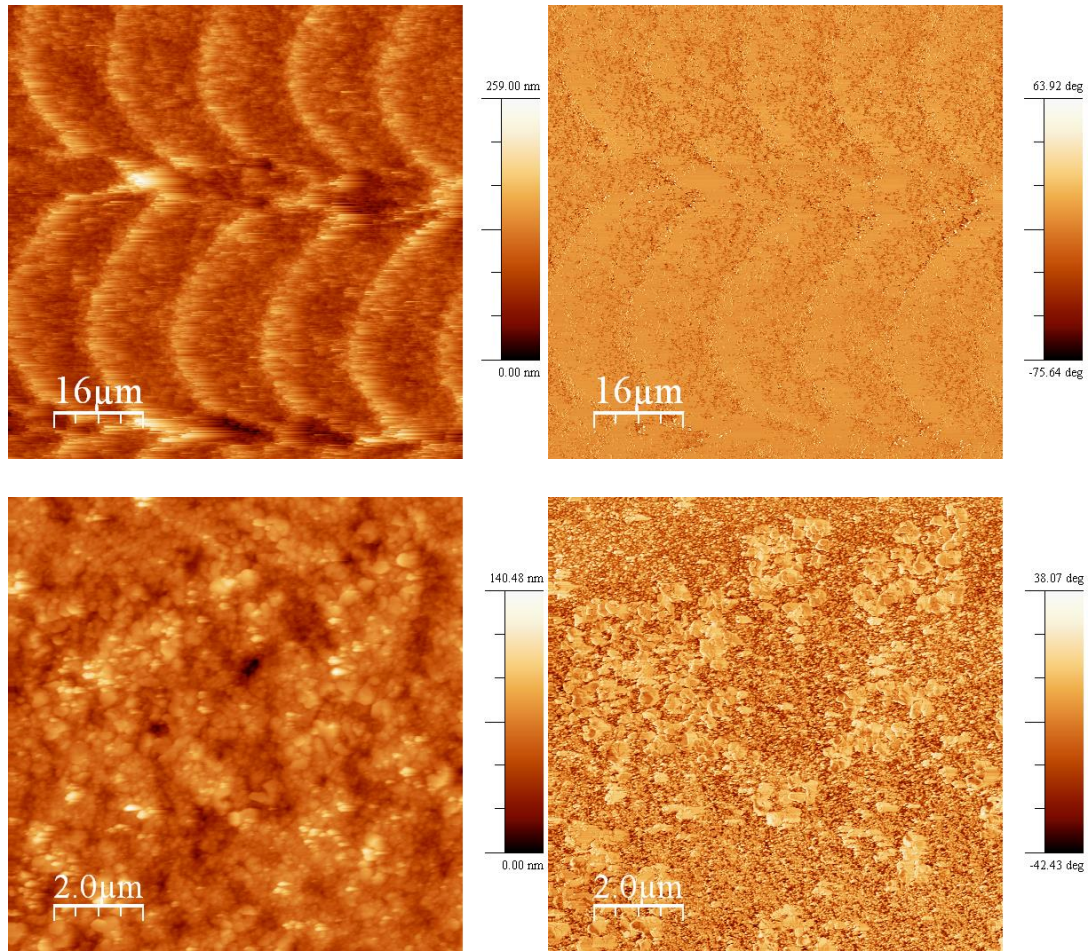


Figure S 26. AC-AFM images of TAE-4 surface in complete devices. Topography in the images on the left hand side and phase in the images on the right hand side. From the 80x80 micrometre area topography in the top image, a roughness average of $R_a = 18$ nm and a root mean square average roughness of $RMS = 22$ nm can be obtained. From the 10x10 micrometre area topography in the bottom image, a roughness average of $R_a = 12$ nm and a root mean square average roughness of $RMS = 15$ nm can be obtained.

9. XRD analysis of complete devices

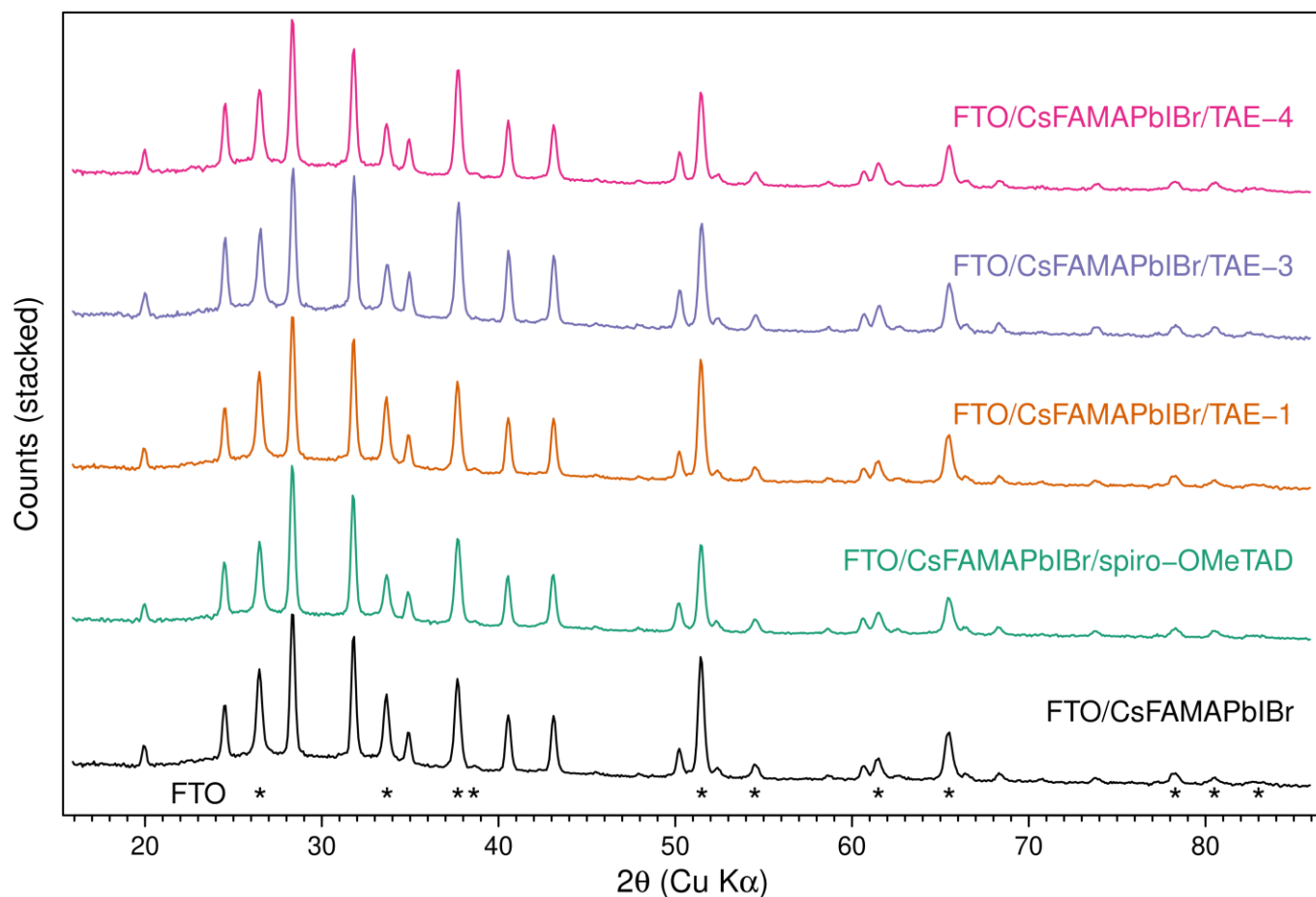


Figure S 27. The XRD pattern measured on complete devices avoiding the area covered with the gold electrode. The amorphous HTMs, the very thick titanium oxide layer, and the gold are not visible in the diffraction pattern. The FTO peaks are visible and marked with an * asterisk. The perovskite pattern is identical to the Cs5 reference pattern from ¹⁶. The diffraction pattern of the devices have been measured at least 8 months after their fabrication. The fact that no significant difference can be observed between the perovskite below any of the HTMs and the uncovered perovskite, supports the absence of chemical reactivity between the HTMs and the perovskite layer.

10. Perovskite Layer Thickness Evaluation via Elevation Profile Measurement

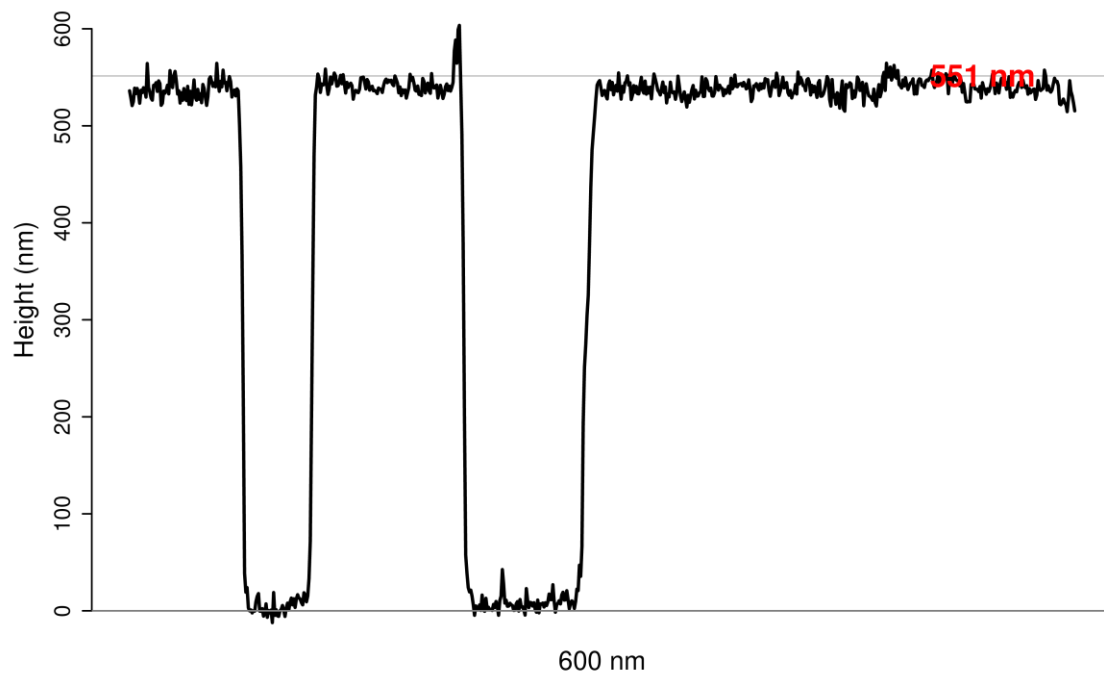
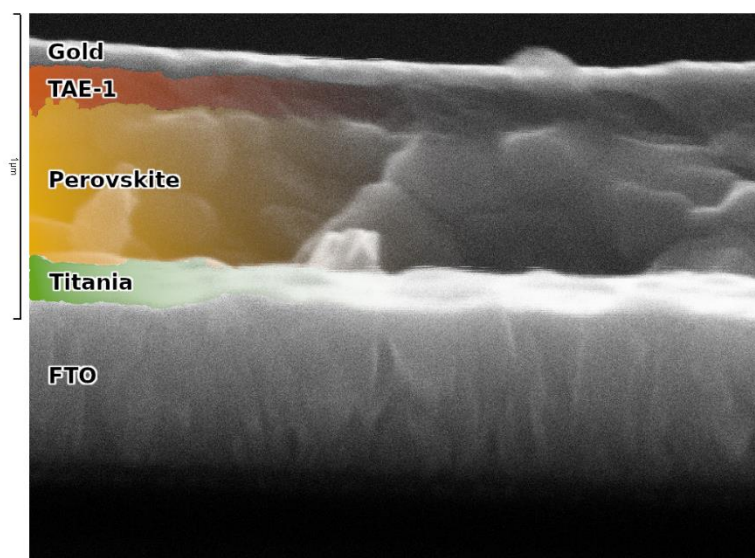
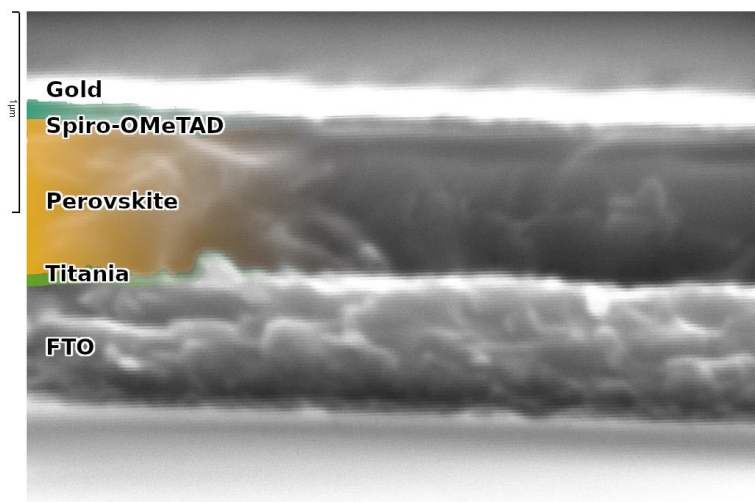


Figure S 28. The elevation profile of a mechanically furrowed perovskite layer not covered by any HTM. The underlying dense titanium oxide layer is hard enough to not be scratched. The measurement was performed with a calibrated stylus profilometer.

11. Cross-sectional characterization via Scanning Electron Microscopy (SEM)



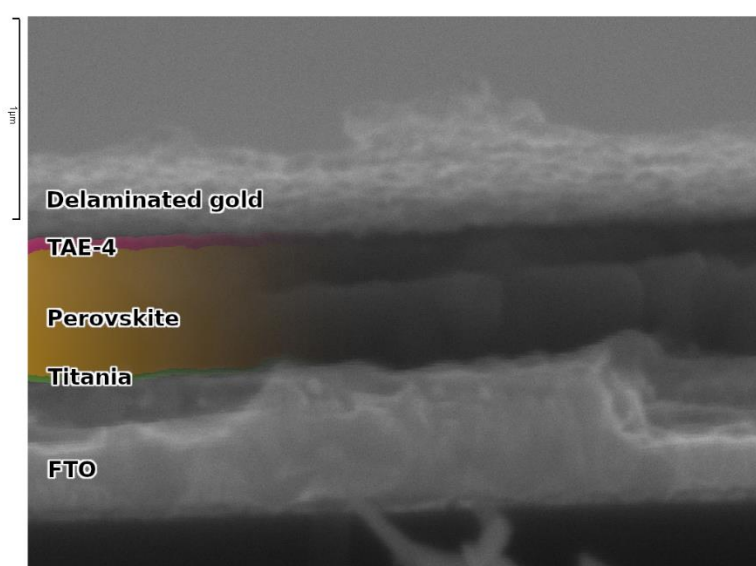
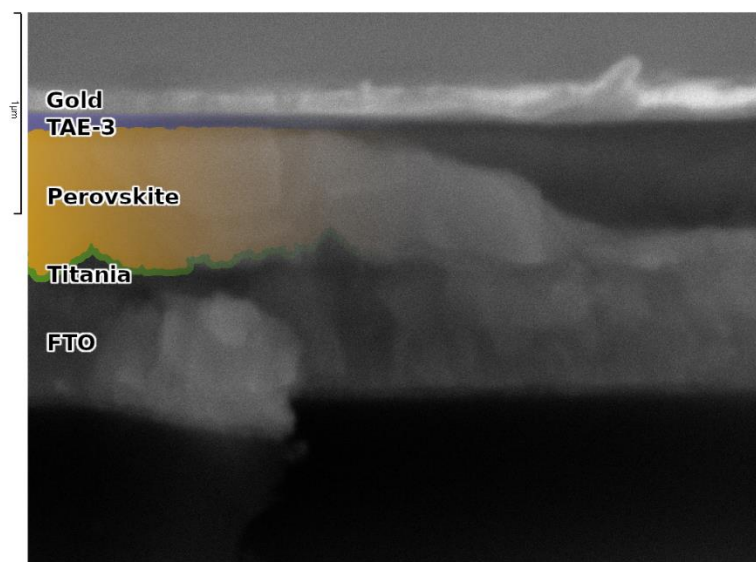
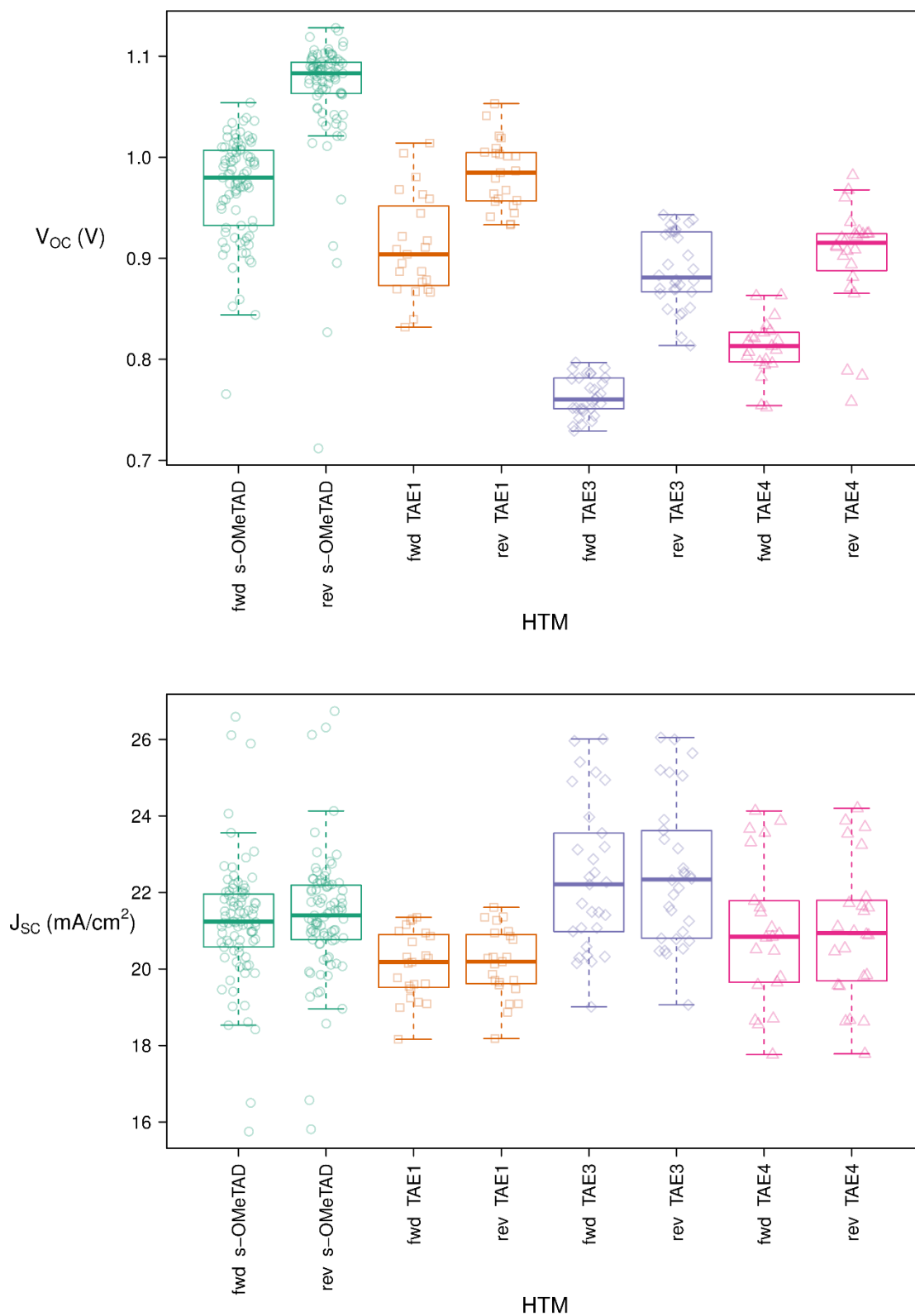


Figure S 29. Cross-section images acquired with an ESEM equipment at high vacuum and 20 kV accelerated electron beam. Full devices with spiro-OMeTAD (first), TAE-1 (second), TAE-3 (third) and TAE-4 (fourth). The scale bar corresponds to 1 μm .

12. Device statistics



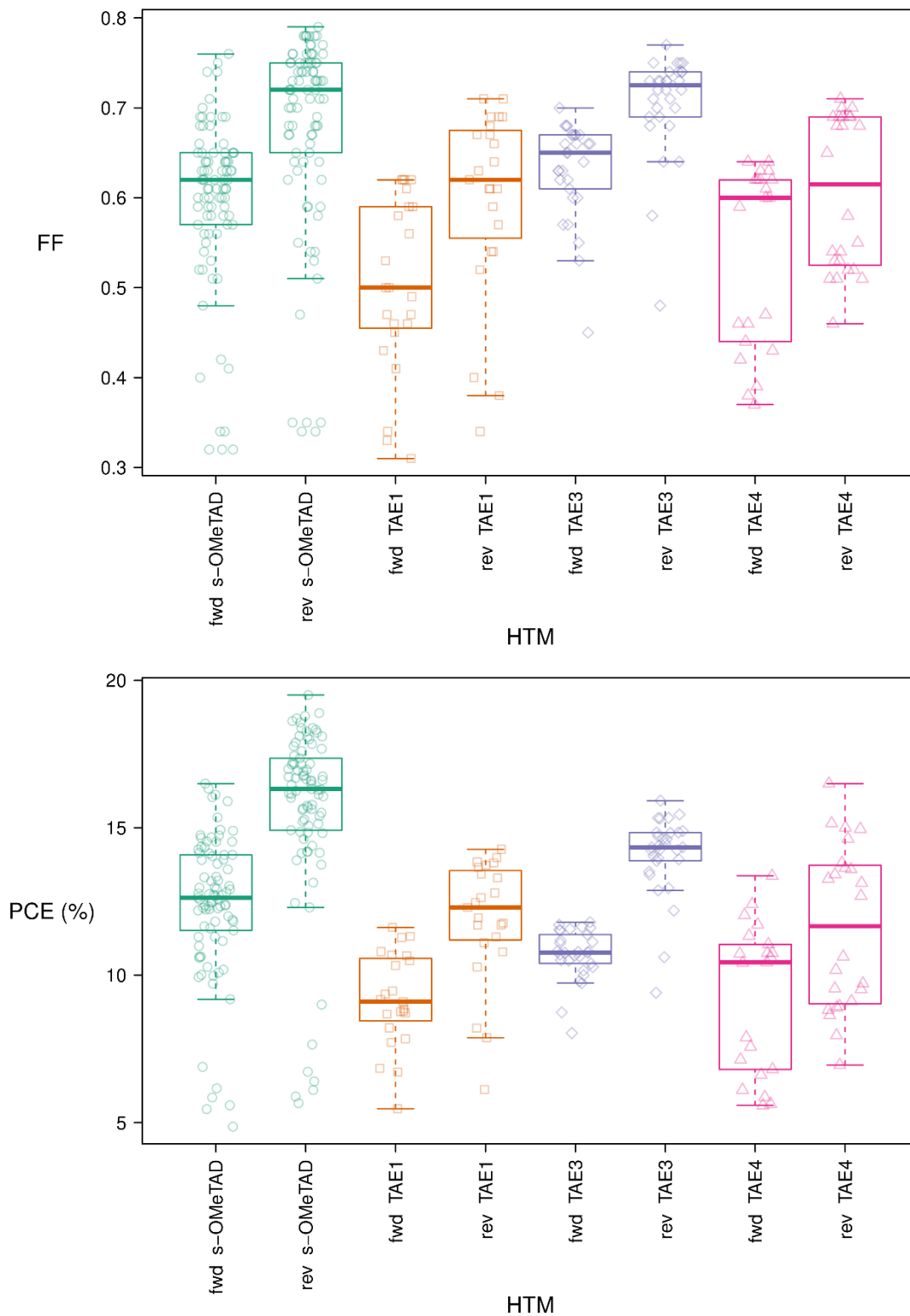


Figure S 30. Device statistics (from top to bottom: open circuit voltage, short circuit current, fill factor, power conversion efficiency) for all devices of spiro-OMeTAD (85 independent diodes), TAE-1 (23 independent diodes), TAE-3 (29 independent diodes) and TAE-4 (21 independent diodes) used in this study.

13. Forward and Reverse Current-voltage Scans for Champion Devices

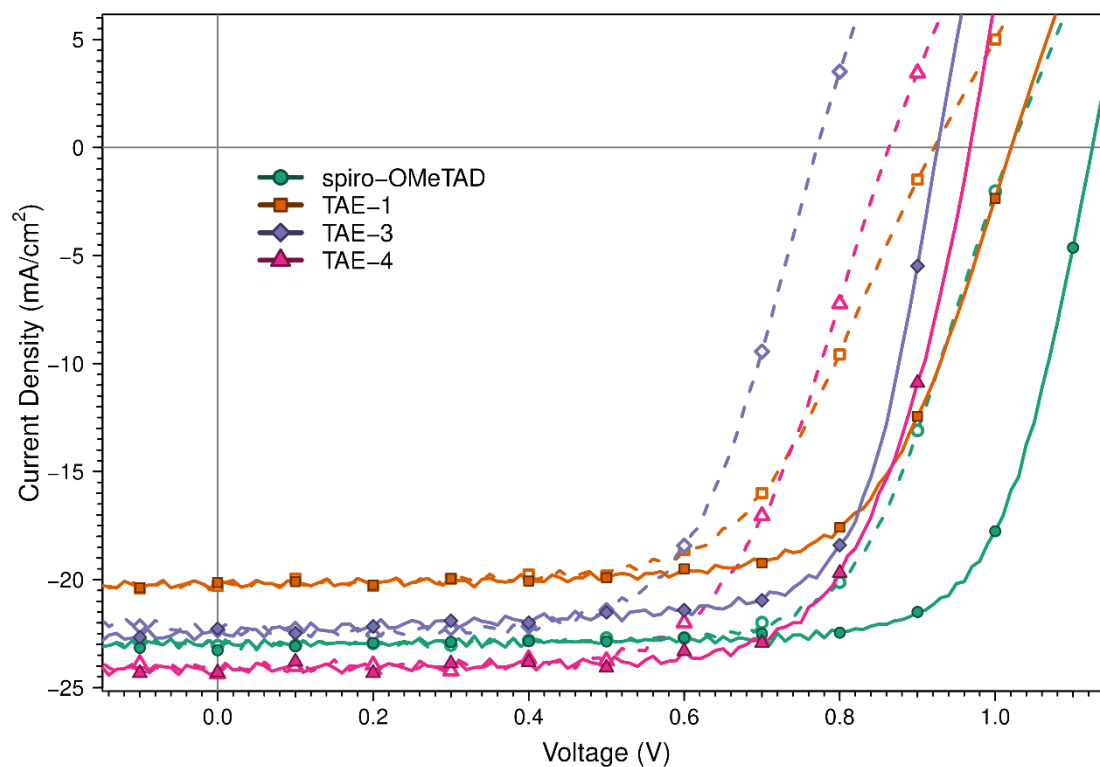


Figure S 31. Forward (dashed) and reverse (solid) current-voltage curves for the most efficient spiro-OMeTAD (green), TAE-1 (orange), TAE-3 (purple) and TAE-4 (magenta) devices. All devices were measured using same conditions (illumination at AM 1.5, 0.6 V/s). The noise observed in the profile is mainly caused by small fluctuations in the illumination intensity.

14. Current-voltage Scans at Different Sweep Speeds

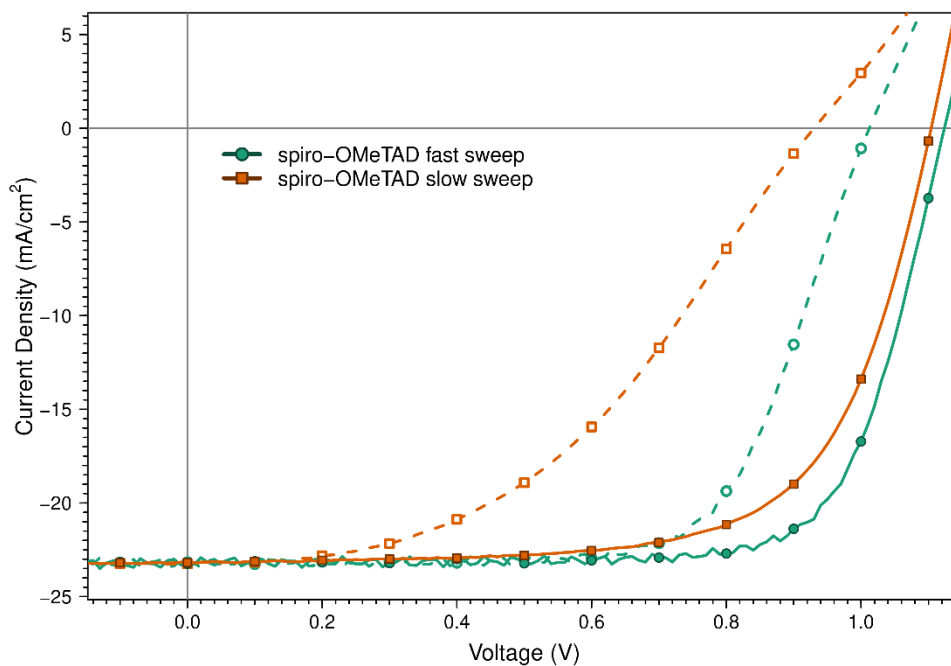


Figure S 32. A current-voltage scan of a device with spiro-OMeTAD as HTM. Fast sweep were performed at 600 mV/s while slow sweeps were performed at 30 mV/s.

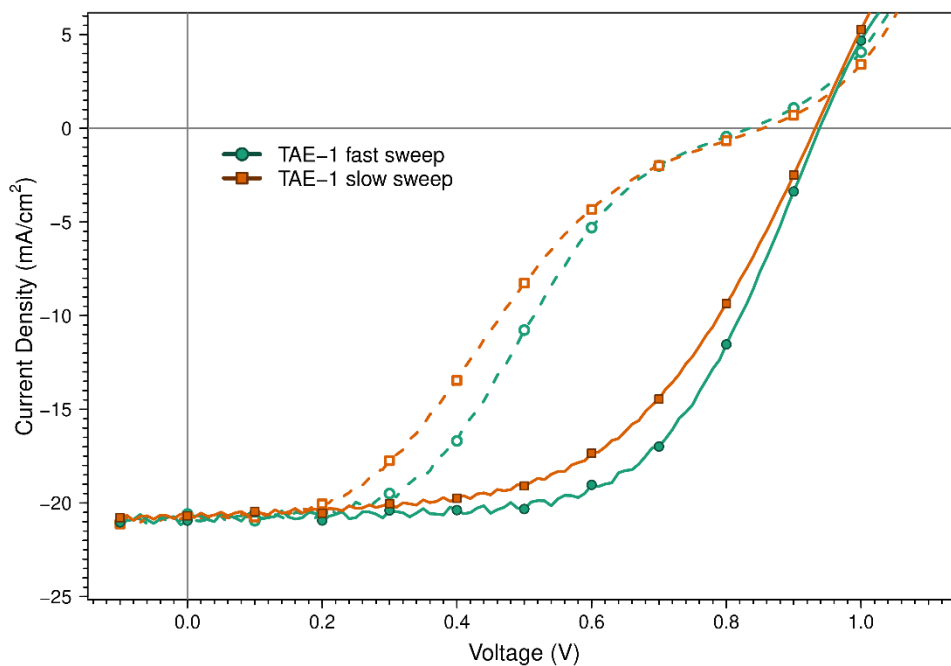


Figure S 33. A current-voltage scan of a device with TAE-1 as HTM. Fast sweep were performed at 600 mV/s while slow sweeps were performed at 300 mV/s.

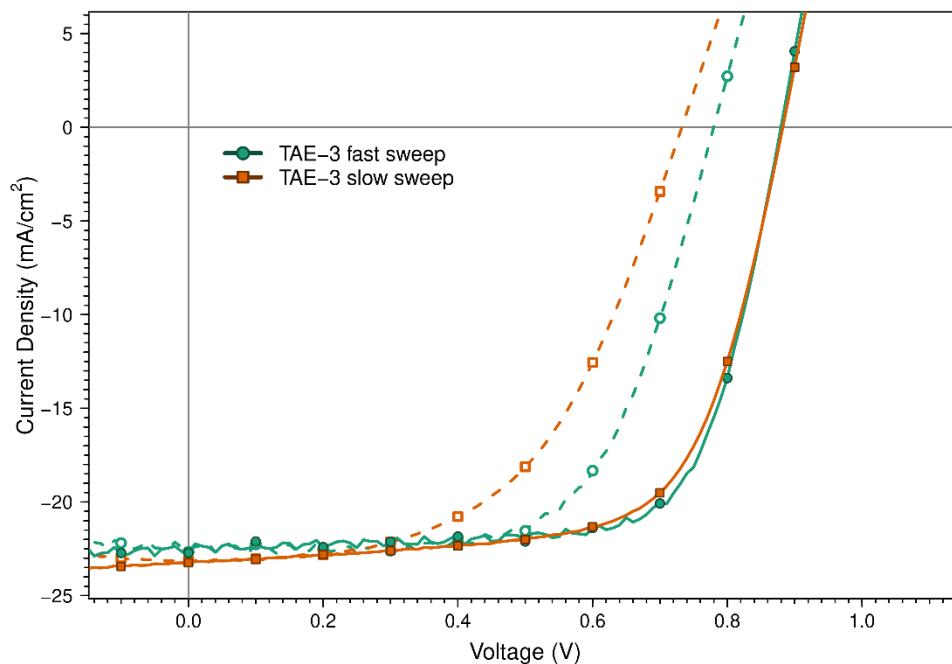


Figure S 34. A current-voltage scan of a device with TAE-3 as HTM. Fast sweep were performed at 600 mV/s while slow sweeps were performed at 80 mV/s.

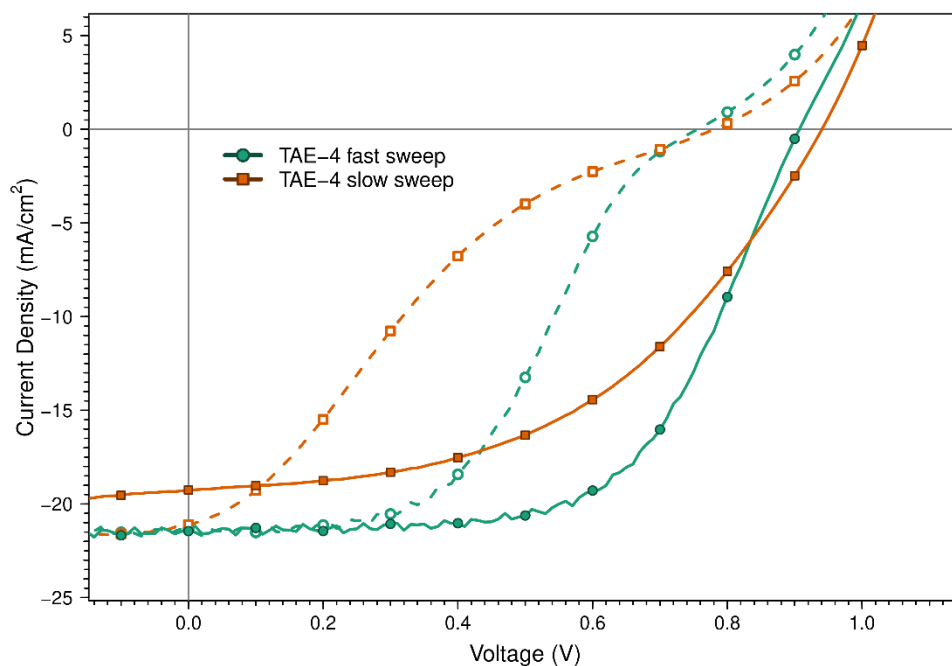


Figure S 35. A current-voltage scan of a device with TAE-4 as HTM. Fast sweep were performed at 600 mV/s while slow sweeps were performed at 30 mV/s.

15. Current-voltage Scans at Different Illumination Intensities

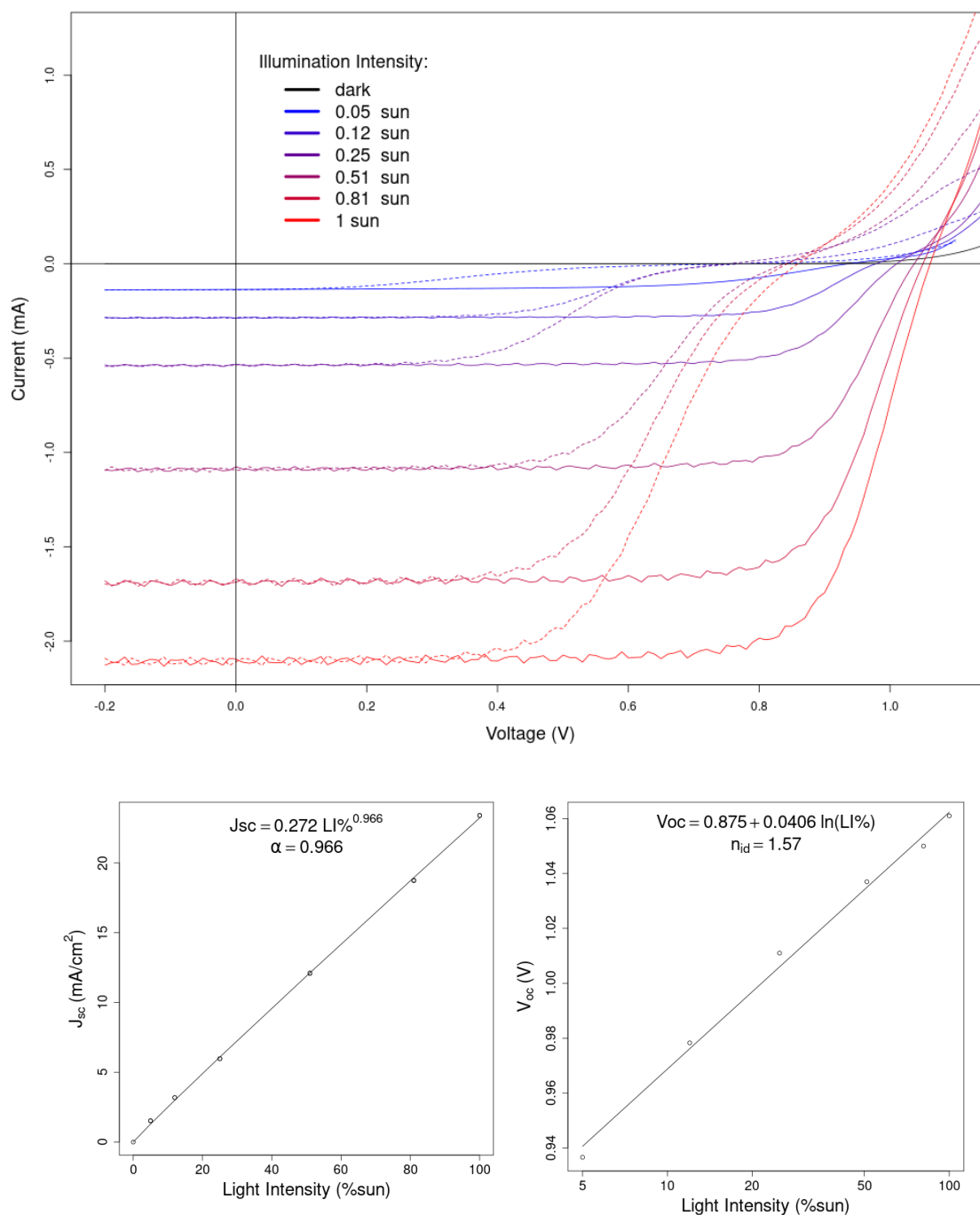


Figure S 36. Current-voltage scans of a perovskite solar cell with **spiro-OMeTAD** as HTM attenuating the solar simulator illumination with filters, scan speed 0.6 V/s: (top) forward (dashed) and reverse (solid); (bottom left) power law fitting of the short circuit current at different light intensity; (bottom right) linear fitting of the reverse scan open circuit voltage versus the natural logarithm of the light intensity, and the obtained ideality factor.

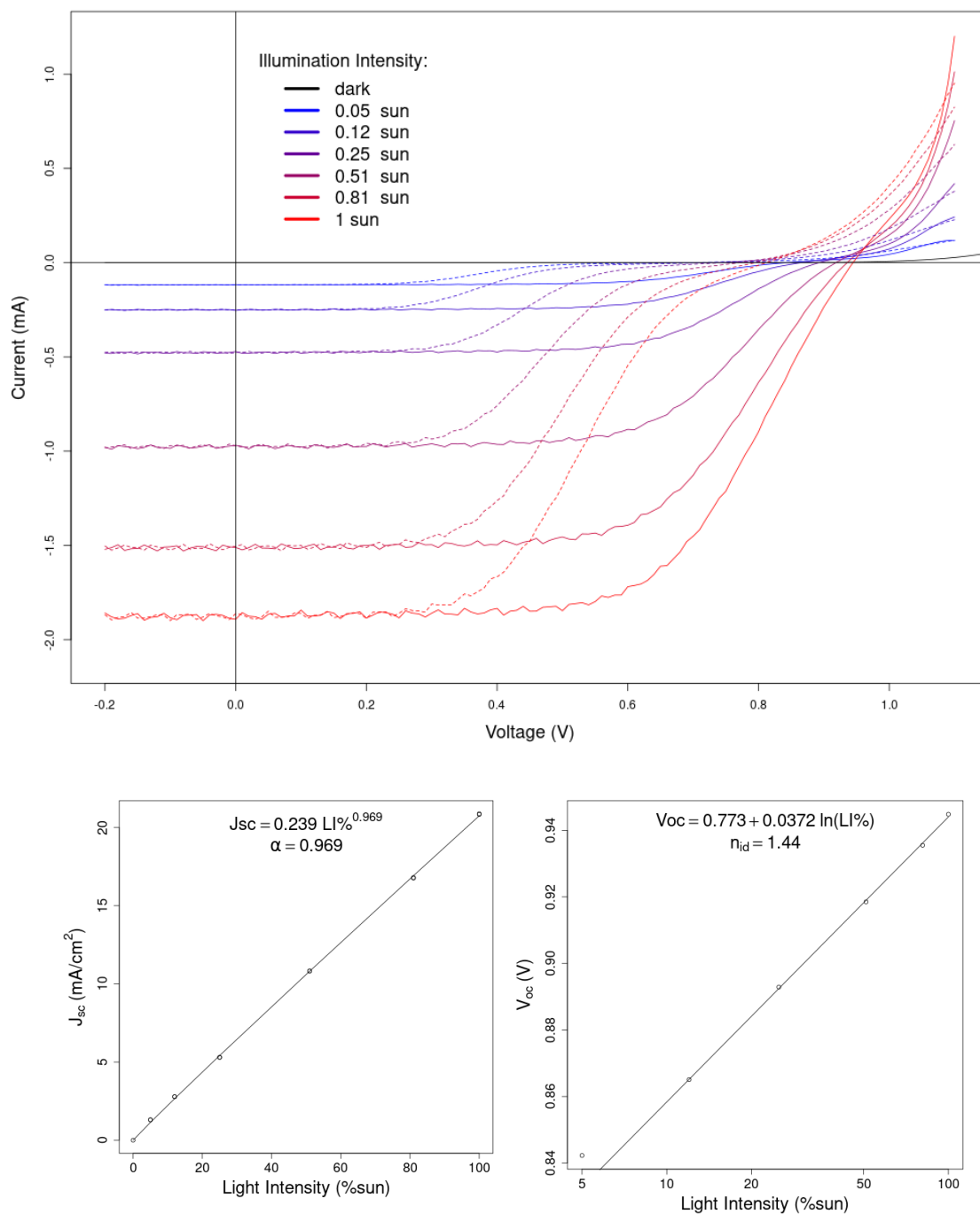


Figure S 37. Current-voltage scans of a perovskite solar cell with **TAE-1** as HTM attenuating the solar simulator illumination with filters, scan speed 0.6 V/s: (top) forward (dashed) and reverse (solid); (bottom left) power law fitting of the short circuit current at different light intensity; (bottom right) linear fitting of the reverse scan open circuit voltage versus the natural logarithm of the light intensity, and the obtained ideality factor.

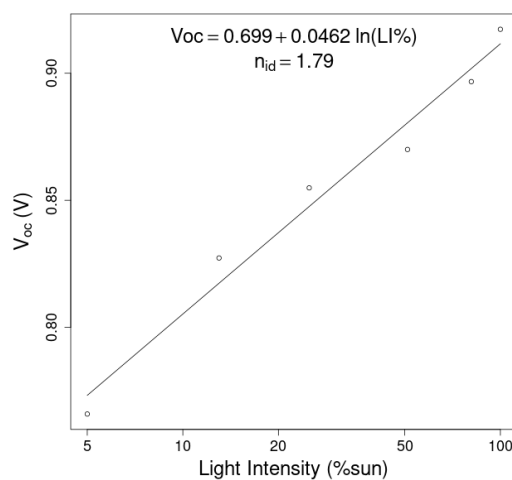
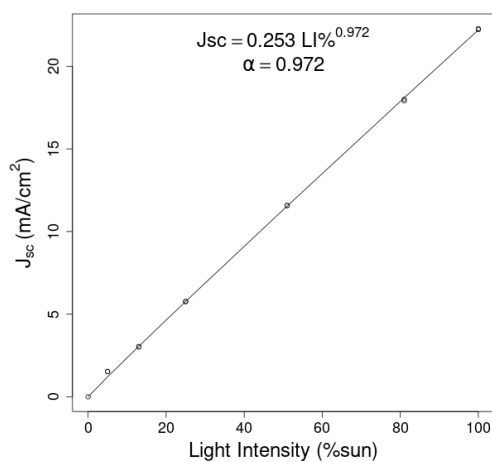
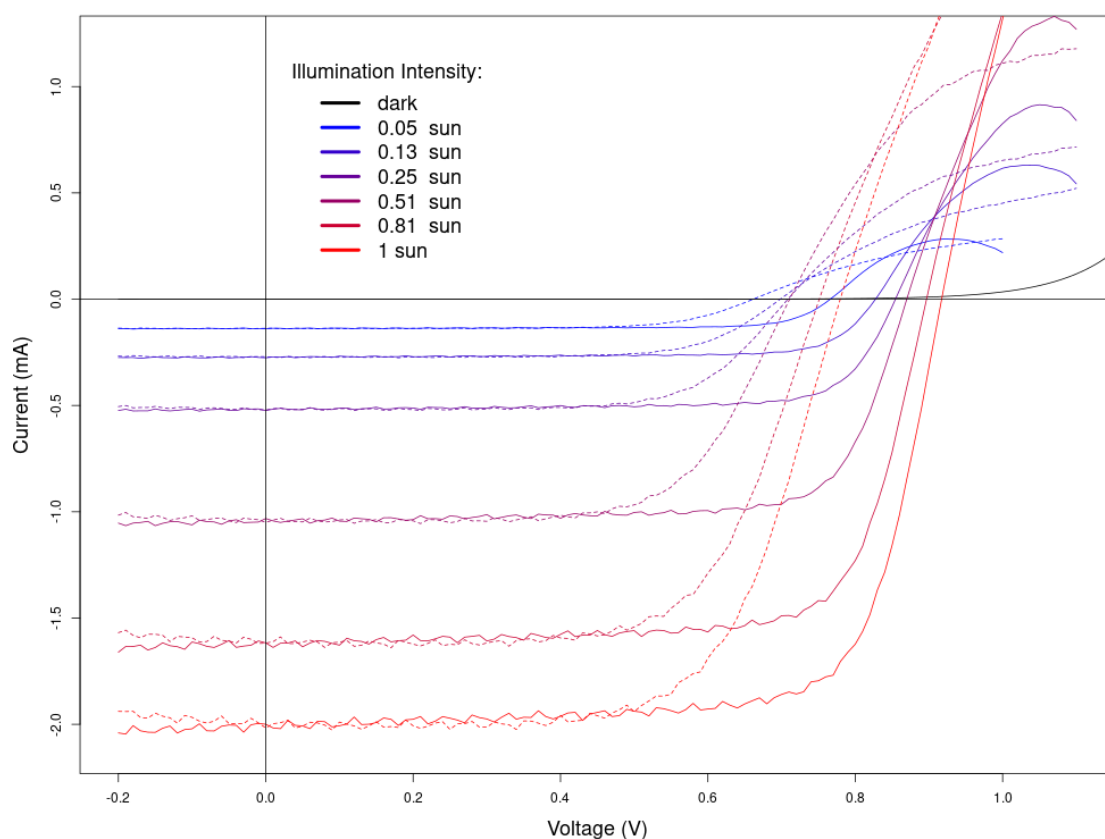


Figure S 38. Current-voltage scans of a perovskite solar cell with **TAE-3** as HTM attenuating the solar simulator illumination with filters, scan speed 0.6 V/s: (top) forward (dashed) and reverse (solid); (bottom left) power law fitting of the short circuit current at different light intensity; (bottom right) linear fitting of the reverse scan open circuit voltage versus the natural logarithm of the light intensity, and the obtained ideality factor.

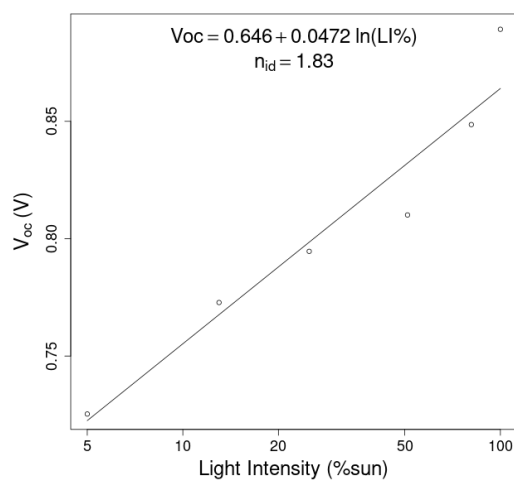
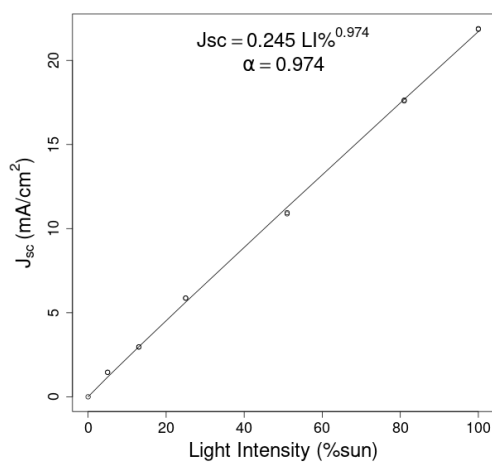
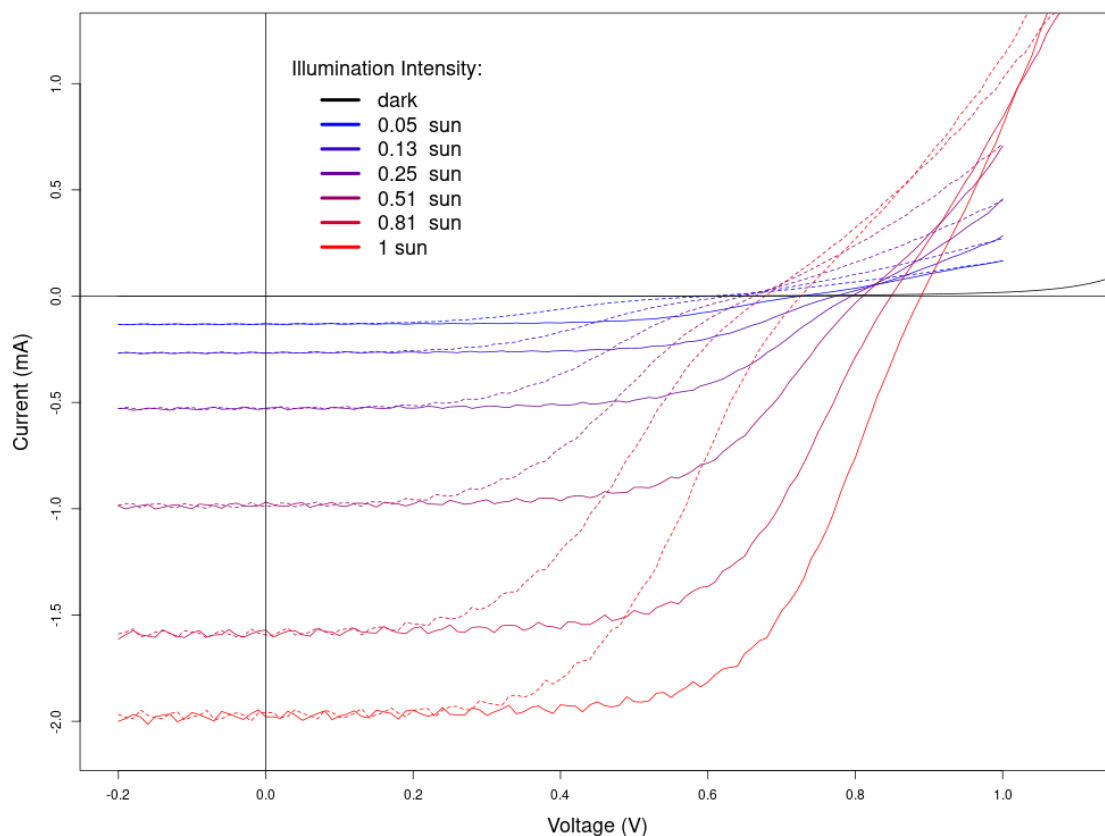
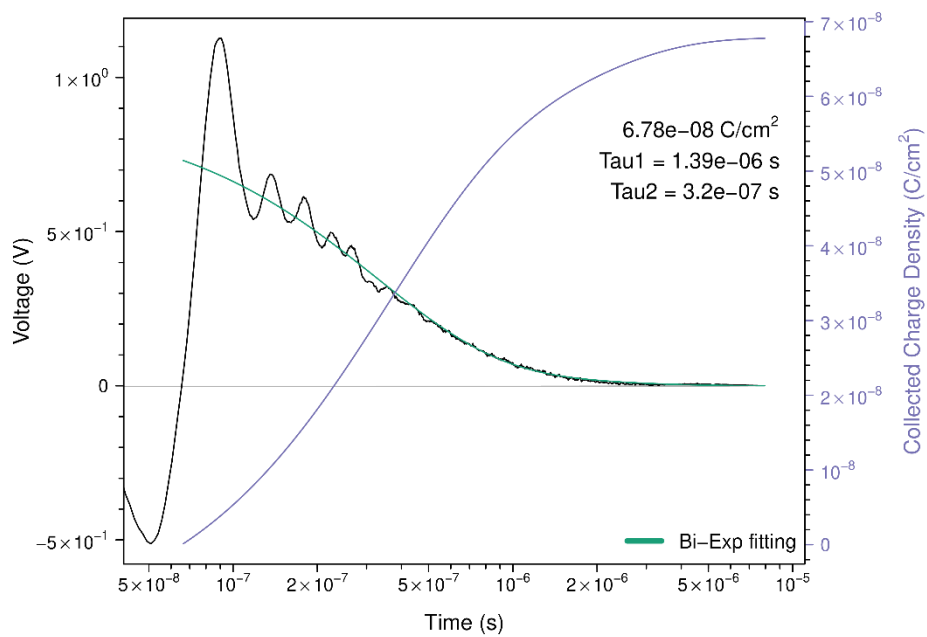
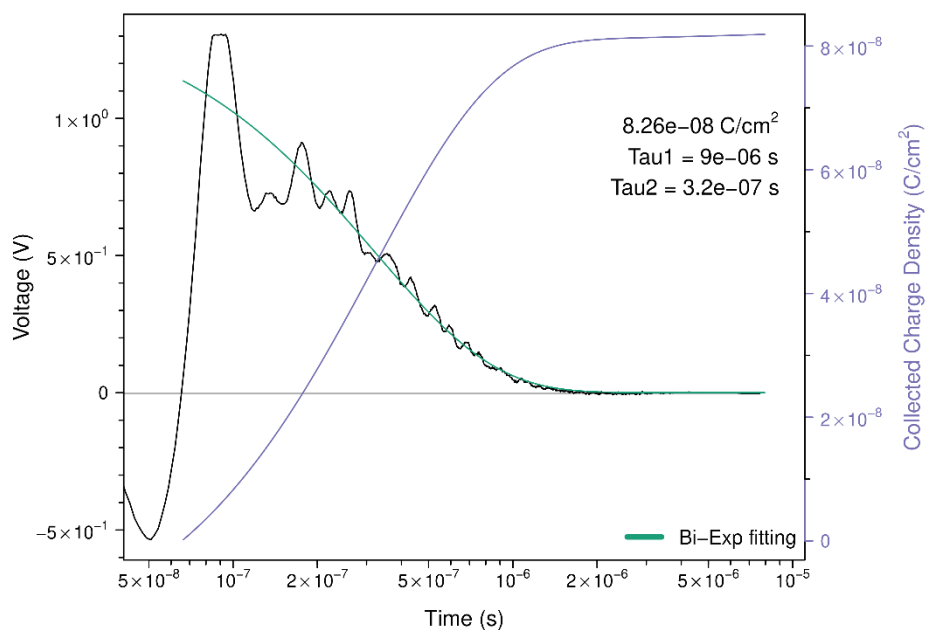


Figure S 39. Current-voltage scans of a perovskite solar cell with **TAE-4** as HTM attenuating the solar simulator illumination with filters, scan speed 0.6 V/s: (top) forward (dashed) and reverse (solid); (bottom left) power law fitting of the short circuit current at different light intensity; (bottom right) linear fitting of the reverse scan open circuit voltage versus the natural logarithm of the light intensity, and the obtained ideality factor.

16. Photo-induced time-resolve measurements



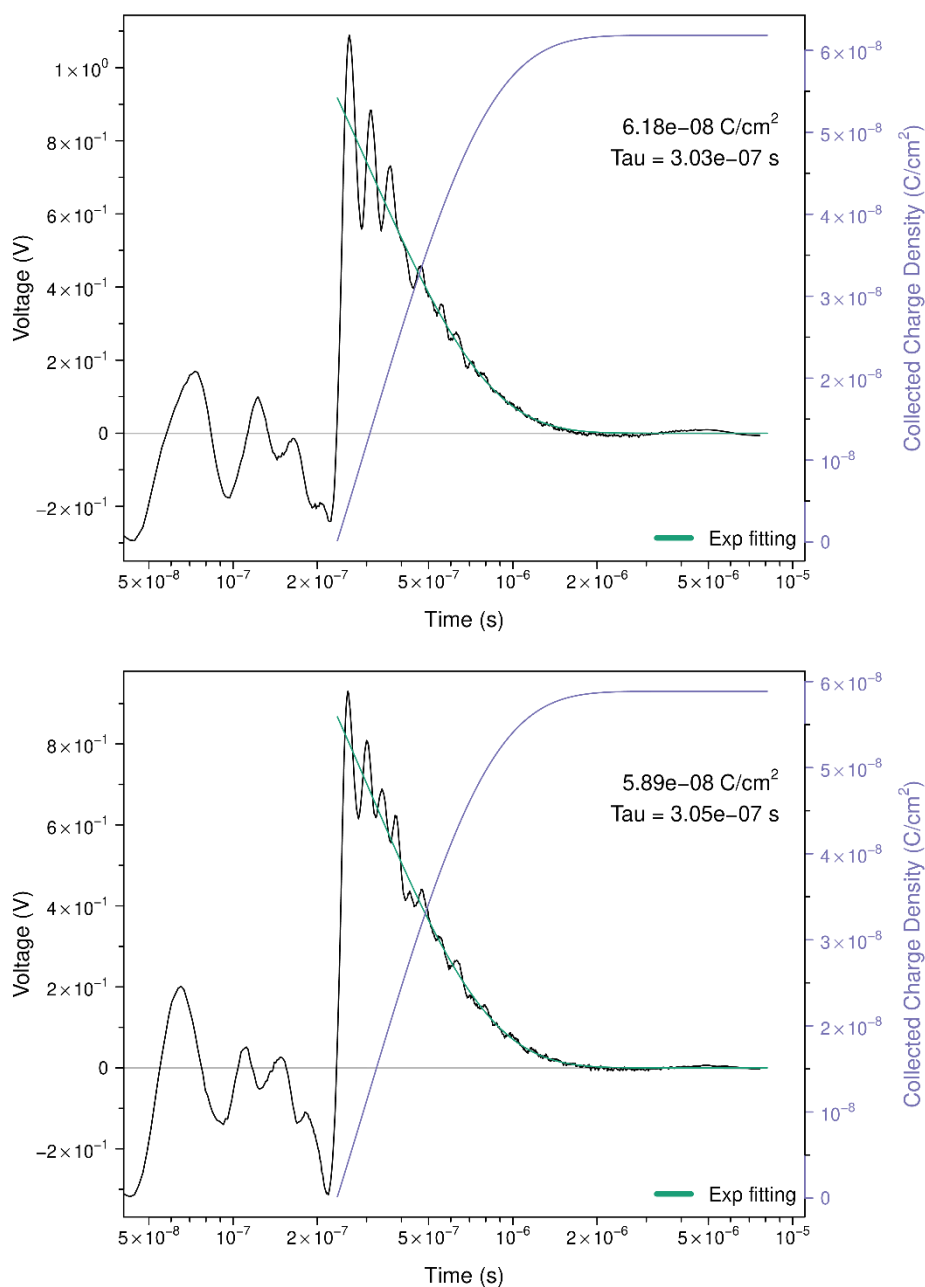
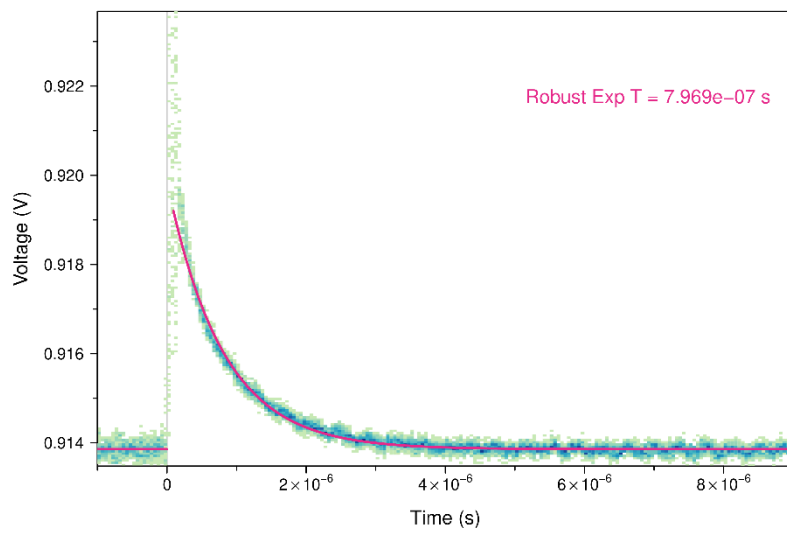
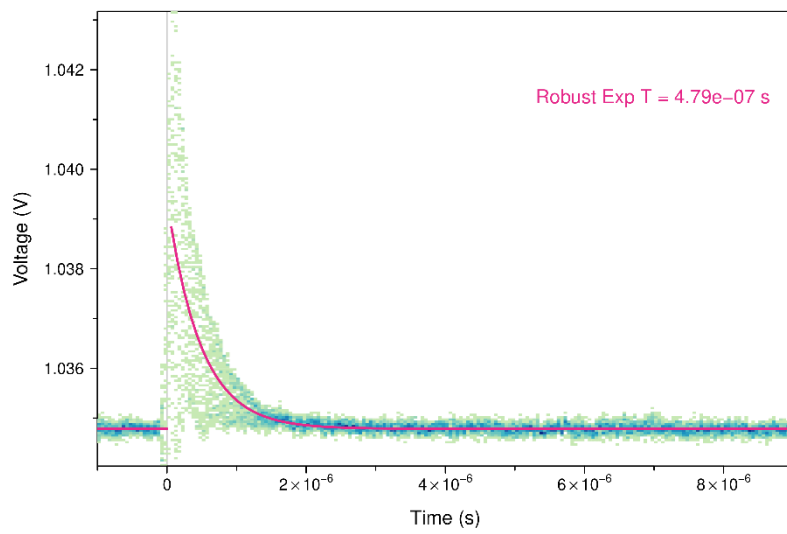
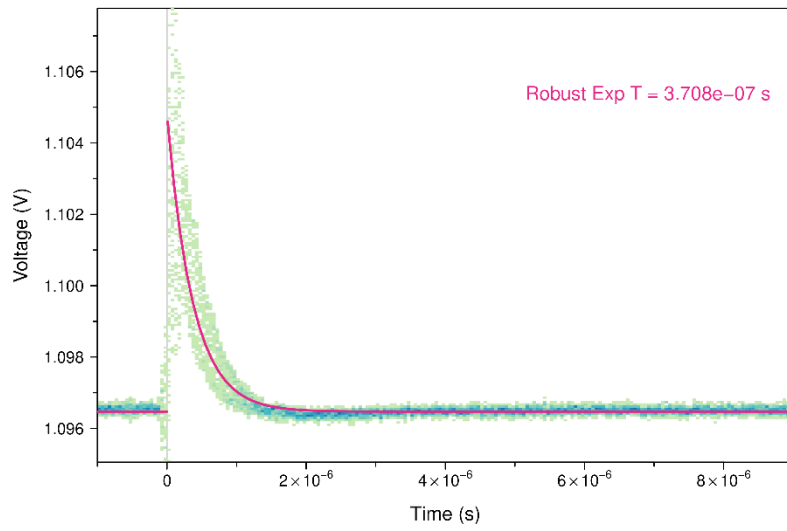


Figure S 40. Charge extraction profile (CE, black) at 1 sun equivalent illumination (lower illuminations have been measured but the full decay is not reported here) for (first) spiro-OMeTAD, (second) TAE-1, (third) TAE-3 and (fourth) TAE-4. The voltage profile can be converted to a current profile dividing by the external circuit resistance of 50Ω . In grey the baseline for integration. In green the fitting with an exponential or a bi-exponential decay (sum of two exponential decays) as indicated in the legend. The exponential fitting was employed in the cases where bi-exponential fitting was not converging. In any case robust fitting was performed, as implemented in R/robustbase/nlrob.¹⁷ In purple the integral of the fit. The whole procedure can be seen in <https://github.com/ilario/photophysics-data-processing-R/blob/master/ce-integrateExp.R>



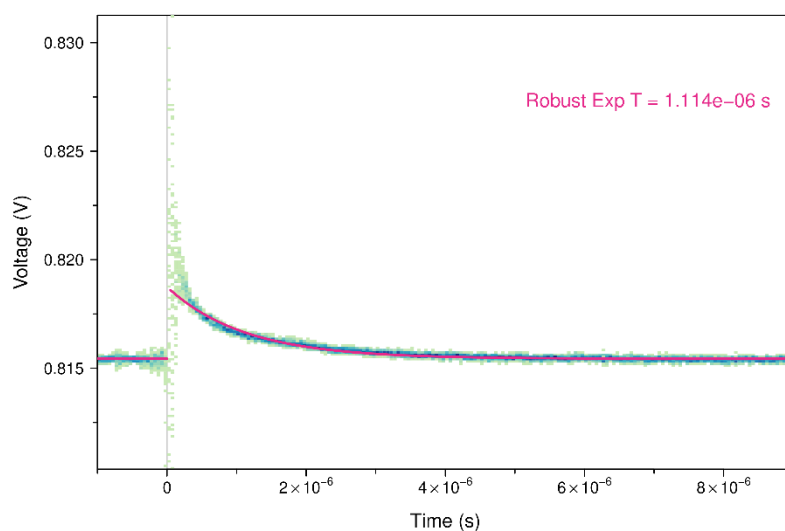


Figure S 41. Transient voltage decays from TPV (monitoring the V_{OC} profile evolution of a complete device after a perturbation via a laser pulse) of devices with (first) spiro-OMeTAD, (second) TAE-1, (third) TAE-3 and (fourth) TAE-4 as HTM. In this case the background illumination was equivalent to 1 sun. In order to limit the overplotting problem, the 12500 data points has been represented as a 2D histogram. The solid purple line represents the robust mono-exponential ($V = V_0 + \Delta V e^{-t/\tau}$) fitting as implemented in R/robustbase/nlrob.¹⁷ The number reported in purple in the plot is the exponential coefficient τ from the fit. Biexponential fit ($V = V_0 + \Delta V_1 e^{-t/\tau_1} + \Delta V_2 e^{-t/\tau_2}$) has also been performed, showing no significant improvement.

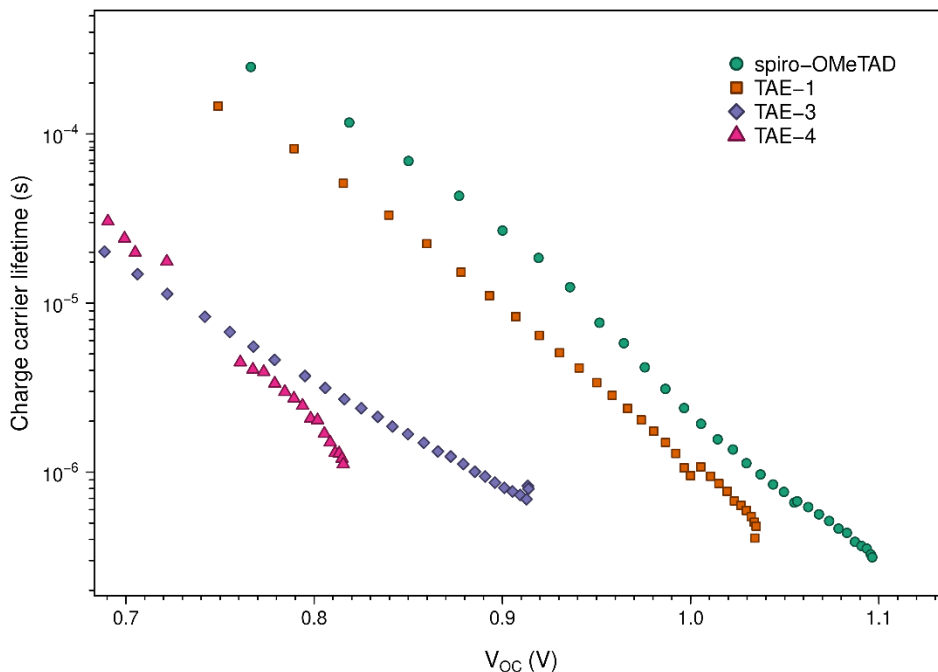


Figure S 42. Charge carrier lifetime at different applied illuminations (TPV). The x axis reports the V_{OC} due to the applied illumination (light bias).

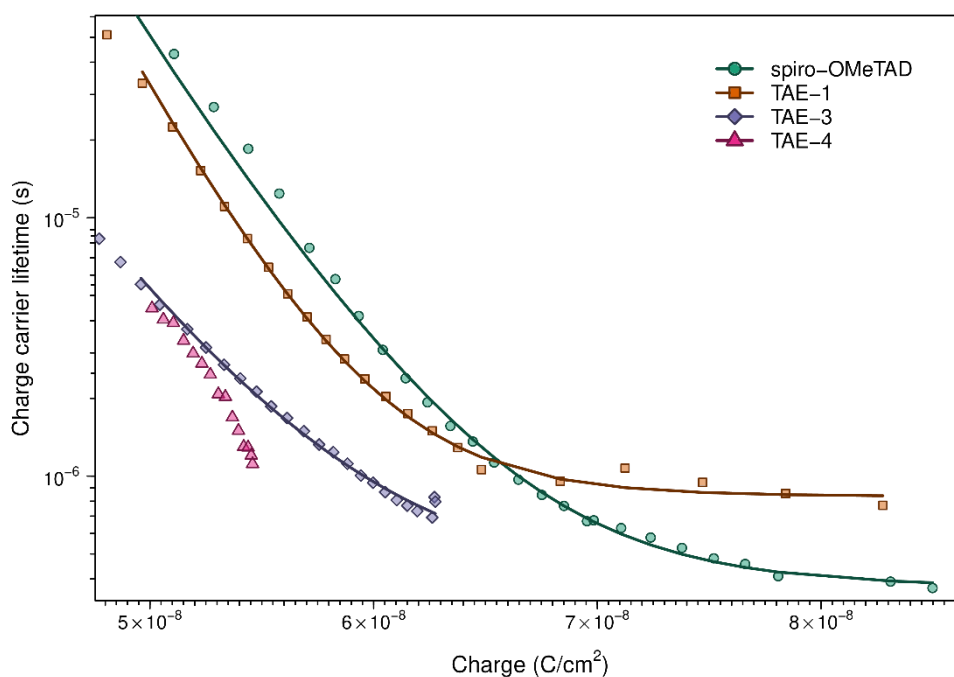


Figure S 43. Charge carrier lifetime (from TPV) plotted versus the total charge obtained via charge extraction (CE, including both charge stored in geometrical and chemical capacitance). The solid lines are power law fitting ($y=y_0+Ax^{-\lambda}$), as shown in the main text, but the recombination orders obtained in this case (considering also the geometrical capacitance charge) are unphysical (16 for spiro-OMeTAD devices, 18 for TAE-1 devices, 13 for TAE-3 devices, and it was not fitted for TAE-4).

17. Contact potential difference measurements for work function determination

Electrostatic force measurements were performed by means of an Scanning Probe Microscope to evaluate the contact potential difference between a metallic tip and the sample. The contact potential difference, CPD or V_{CPD} , can be measured from the parabolic dependence of the electrostatic force with the tip-sample applied bias. In dynamic electrostatic force measurements, an oscillating tip is not in direct contact with the sample but electrically connected via electronics, causing the alignment of their Fermi levels and, therefore, creating a CPD between tip and sample. If the work function of the tip (vibrating electrode) is ϕ_{tip} and ϕ_{sample} is that of the sample, then the contact potential difference between tip and sample is:

$$V_{CPD} = \frac{\phi_{tip} - \phi_{sample}}{-e} = \Delta\phi_s / e \quad (1)$$

where e is the electric charge. Due to this CPD, an electrostatic force is developed which has a parabolic dependence with the tip-sample bias voltage. As the frequency or phase shift of the oscillating probe is proportional to the force gradient, it will also present the same dependence:

$$\Delta f(V) = -\frac{f_0}{4k} \frac{\partial^2 C(z)}{\partial z^2} (V - V_{CPD})^2 \quad (2)$$

where f_0 , k , z , $C(z)$ and V_{CPD} are, respectively, the resonance frequency, spring constant, distance, capacitance and contact potential difference of the tip-sample system and $\Delta f(V)$ is the magnitude measured. Thus, in principle, knowing the work function of the tip (ϕ_{tip}), the work function of the sample (ϕ_{sample}) can be calculated from (1). However, in order to avoid uncertainties related to the tip conditions or material, having an in-situ reference is convenient. The use of such a reference also permits reliable comparison between different samples. In the present case, this reference is provided by a gold electrode deposited on top of each surface layer. In such a way, the contact potential difference between the sample and the gold electrode ($\phi = 4.9$ eV)⁵ permits evaluating the sample work function independently of the material the tip is made of:

$$\Delta\phi = \phi_{sample} - \phi_{Au} = e [V_{CPD}(sample) - V_{CPD}(Au)] \quad (3)$$

To obtain $\Delta\phi$ we perform spectroscopic curves: direct measurement of $\Delta f(V)$ by obtaining the frequency shift versus applied bias over specific surface locations. The robustness of the method and reproducibility of the results are verified by statistical analysis of measurements taken on diverse locations and several curves obtained at each position. As a measure of the precision, errors for each case are estimated as the standard deviation of the mean: $SDOM = \pm \sigma/\sqrt{n}$, where σ is the standard deviation of the data and n is the number of data values.

18. Supplementary references

- 1 L. Cabau, I. Garcia-Benito, A. Molina-Ontoria, N. F. Montcada, N. Martin, A. Vidal-Ferran and E. Palomares, *Chem. Commun.*, 2015, **51**, 13980–13982.
- 2 I. Horcas, R. Fernández, J. M. Gómez-Rodríguez, J. Colchero, J. Gómez-Herrero and A. M. Baro, *Rev. Sci. Instrum.*, 2007, **78**, 013705.
- 3 P. N. Murgatroyd, *J. Phys. D. Appl. Phys.*, 1970, **3**, 308.
- 4 J. A. Röhr, D. Moia, S. A. Haque, T. Kirchartz and J. Nelson, *J. Phys. Condens. Matter*, 2018, **30**, 105901.
- 5 I. D. Baikie, A. C. Grain, J. Sutherland and J. Law, *Appl. Surf. Sci.*, 2014, **323**, 45–53.
- 6 M. W. Wong, K. B. Wiberg and M. J. Frisch, *J. Am. Chem. Soc.*, 1992, **114**, 1645–1652.
- 7 F. Weigend and R. Ahlrichs, *Phys. Chem. Chem. Phys.*, 2005, **7**, 3297.
- 8 M. J. Frisch, G. W. Trucks, H. B. Schlegel, G. E. Scuseria, M. A. Robb, J. R. Cheeseman, G. Scalmani, V. Barone, G. A. Petersson, H. Nakatsuji, X. Li, M. Caricato, A. V. Marenich, J. Bloino, B. G. Janesko, R. Gomperts, B. Mennucci, H. P. Hratchian, J. V. Ortiz, A. F. Izmaylov, J. L. Sonnenberg, Williams, F. Ding, F. Lipparini, F. Egidi, J. Goings, B. Peng, A. Petrone, T. Henderson, D. Ranasinghe, V. G. Zakrzewski, J. Gao, N. Rega, G. Zheng, W. Liang, M. Hada, M. Ehara, K. Toyota, R. Fukuda, J. Hasegawa, M. Ishida, T. Nakajima, Y. Honda, O. Kitao, H. Nakai, T. Vreven, K. Throssell, J. A. Montgomery Jr., J. E. Peralta, F. Ogliaro, M. J. Bearpark, J. J. Heyd, E. N. Brothers, K. N. Kudin, V. N. Staroverov, T. A. Keith, R. Kobayashi, J. Normand, K. Raghavachari, A. P. Rendell, J. C. Burant, S. S. Iyengar, J. Tomasi, M. Cossi, J. M. Millam, M. Klene, C. Adamo, R. Cammi, J. W. Ochterski, R. L. Martin, K. Morokuma, O. Farkas, J. B. Foresman and D. J. Fox, *Gaussian 09 (Gaussian Inc., Wallingford, CT)*.
- 9 B. Balakrishna, A. Bauzá, A. Frontera and A. Vidal-Ferran, *Chem. - A Eur. J.*, 2016, **22**, 10607–10613.
- 10 G. Scalmani and M. J. Frisch, *J. Chem. Phys.*, 2010, **132**, 114110.
- 11 A. V. Marenich, C. J. Cramer and D. G. Truhlar, *J. Phys. Chem. B*, 2009, **113**, 6378–6396.
- 12 S. Kupfer, J. Guthmuller and L. González, *J. Chem. Theory Comput.*, 2013, **9**, 543–554.
- 13 T. Yanai, D. P. Tew and N. C. Handy, *Chem. Phys. Lett.*, 2004, **393**, 51–57.
- 14 N. M. O'boyle, A. L. Tenderholt and K. M. Langner, *J. Comput. Chem.*, 2008, **29**, 839–845.
- 15 B. Wang, Z. Xie, Y. Li, Z. Yang and L. Chen, *Macromolecules*, 2018, **51**, 3443–3449.
- 16 M. Saliba, T. Matsui, J.-Y. Seo, K. Domanski, J.-P. Correa-Baena, M. K. Nazeeruddin, S. M. Zakeeruddin, W. Tress, A. Abate, A. Hagfeldt and M. Grätzel, *Energy Environ. Sci.*, 2016, **9**, 1989–1997.
- 17 M. Maechler, P. Rousseeuw, C. Croux, V. Todorov, A. Ruckstuhl, M. Salibian-Barrera, T. Verbeke, M. Koller, E. Concieção and M. A. di Palma, 2018, robustbase: Robust statistics R package 0.93-3.